SWAN: A STUDY OF SOLAR WIND ANISOTROPIES ON SOHO WITH LYMAN ALPHA SKY MAPPING

J.L. BERTAUX[1], E. KYRÖLÄ[2], E. QUÉMERAIS[1], R. PELLINEN[2], R. LALLEMENT[1], W. SCHMIDT[2], M. BERTHÉ[1], E. DIMARELLIS[1], J.P. GOUTAIL[1], C. TAULEMESSE[1], C. BERNARD[1], G. LEPPELMEIER[2], T. SUMMANEN[2], H. HANNULA[3], H. HUOMO[3], V. KEHLÄ[3], S. KORPELA[2,6], K. LEPPÄLÄ[3], E. STRÖMMER[3], J. TORSTI[4], K. VIHERKANTO[3], J.F. HOCHEDEZ, G. CHRETIENNOT[1], R. PEYROUX[1] and T. HOLZER[5]

(1) Service d'Aéronomie du CNRS, BP. 3, 91371, Verrières-le-Buisson, France
(2) Finnish Meteorological Institute, P.O. Box 503, SF. 00101 - Helsinki, Finland
(3)VTT/INS, Technical Research Center of Finland, Espoo and Oulu, Finland
(4) University of Turku, Turku, Finland
(5) High Altitude Observatory, Boulder, Colorado, USA

Abstract. On board the SOHO spacecraft poised at L1 Lagrange point, the SWAN instrument is mainly devoted to the measurement of large scale structures of the solar wind, and in particular the distribution with heliographic latitude of the solar wind mass flux. This is obtained from an intensity map of the sky Lyman α emission, which reflects the shape of the ionization cavity carved in the flow of interstellar H atoms by the solar wind. The methodology, inversion procedure and related complications are described. The subject of latitude variation of the solar wind is shortly reviewed: earlier Lyman α results from Prognoz in 1976 are confirmed by Ulysses. The importance of the actual value of the solar wind mass flux for the equation of dynamics in a polar coronal hole is stressed. The instrument is composed of one electronic unit commanding two identical Sensor Units, each of them allowing to map a full hemisphere with a resolution of 1°, thanks to a two-mirrors periscope system. The design is described in some details, and the rationale for choice between several variants are discussed. A hydrogen absorption cell is used to measure the shape of the interplanetary Lyman α line and other Lyman α emissions. Other types of observations are also discussed : the geocorona, comets (old and new), the solar corona, and a possible signature of the heliopause. The connexion with some other SOHO instruments, in particular LASCO, UVCS, SUMER, is briefly discussed.

Key words: solar wind–interplanetary hydrogen–interstellar wind

1. Introduction

A few months before launch of SOHO spacecraft to Lagrange point L1 is an appropriate time to describe the SWAN instrument, dedicated to the determination of the large scale solar wind distribution by remote sensing in the Lyman α UV light of interplanetary H atoms. The acronym SWAN stands for Solar Wind Anisotropies, where the word anisotropy refers mainly to the variation with latitude of the solar wind. The instrument was built as a co-operative effort between France and Finland, and the name SWAN is particularly appropriate, this white bird being the national bird of Finland. The SWAN investigation is based upon the Lyman α method, which was proven from Prognoz satellite observations in 1976-77. These early observa-

Solar Physics **162**: 403–439, 1995.

TABLE I
SWAN CHARACTERISTICS

Total Mass	13.25 kg
Mass of Electronic Unit	2.82 kg
Mass of one Sensor Unit	4.815 kg
Average Power	11 W
Telemetry	200 bps
Telecommands	69 different TC
Working Temperature	0 to + 30° C
Overall FOV	more than 2π sr for each sensor unit (2-mirror periscope)
Instantaneous FOV	25 pixels of 1 x 1° = 5 x 5°
Wavelength range	115 - 180 nm
Photometric sensitivity	0.75 counts per sec. per Rayleigh per 1° pixel
Type of detector	Solar blind MgF_2/CsI Cathode multianode MCP
Expected count rate	from 200/s (IP) to 10^4/s (solar corona) per pixel
Relative accuracy	better than 1% for 45 sec. counting time on IP signal
Absolute sensitivity	checked at regular time intervals with stellar calibrations
Hydrogen cell	Spectral Resolution : better than 0.01Å (Resolving power 10^5)

tions (together with a 1974 Mariner 10 observation) showing more Lyman α emission near the ecliptic poles than predicted by an isotropic solar wind were demonstrating that the solar wind flux was decreasing with latitude, a fact fully confirmed by the brilliant *in-situ* observations of Ulysses in 1994, out of the ecliptic plane.

Secondary scientific objectives of SWAN include the heliopause signature, the corona, the geocorona, and the monitoring or discovery of comets. Six years after the original SWAN proposal to ESA in 1988, we review the scientific status of the SWAN objectives. The instrument is also described in some details, together with some discussions on the rationale for the selection between several design options. In some sense, SWAN is bridging a gap between the remote sensing coronal instruments of SOHO and their solar wind *in-situ* counterpart. In conjunction with other SOHO instruments, and in particular with UVCS, LASCO, CDS and SUMER, the SWAN investigation will contribute to a better understanding of the generation, acceleration and distribution of the solar wind in the 3D heliosphere.

The instrument characteristics of SWAN are summarized in Table 1.

2. Solar Wind Imprint on the Interstellar H Flow

2.1. The Importance of Solar Wind Mass Flux Measurements

In this section we will rely on a recent review of the connection between the interstellar gas in the heliosphere and the solar wind anisotropies [Lallement *et al.* , 1995].

One of the important unanswered questions in solar physics (and one of the main objectives of the SOHO mission) is the fast solar wind acceleration process. What type of energy (thermal or non-thermal) is transported from the convection zone to above the critical point [Holzer and Leer, 1980; Leer *et al.* , 1982] and how? The classical Parker thermal model succeeds in explaining terminal velocities of up to about 250 km/s, but it fails to reproduce high-speed streams. The coronal base thermal pressure alone is unable to lift up streams carrying up to 4 to 10 times more energy (velocity increase by a factor of 2 to 3.5) than the slow wind. It is well established now that fast solar wind (> 400 km/s) flows from coronal holes, and slow wind from elsewhere on the Sun. Polar coronal holes, sources of the high speed wind around the minimum of activity, are extended and stable for months, and certainly easier to study as compared with equatorial coronal holes (figure 1).

Models devoted to the study of the solar wind acceleration use average ecliptic mass fluxes as boundary conditions for the expansion. However, if the high speed wind mass fluxes were significantly smaller, the dynamics in the acceleration region and the way different types of acceleration models account for it are certainly changed. In particular, the observational evidence, from white-light coronagraphy, for the existence of a non thermal energy flux that emanates from the coronal base [Munro and Jackson, 1977] is strongly dependent on the polar mass flux amplitude (from Lallement, Holzer, Munro, 1986). This means that the latter is a crucial parameter. From the observational point of view, the question of the amplitude of the mass flux from the open field regions, and mainly the polar coronal holes, is still a matter of debate. The Ulysses results have provided the first direct measurement of the high latitude mass flux which was indeed found smaller than in the ecliptic, but earlier Lyman α observations had suggested already a lower solar flux outside the ecliptic plane.

2.2. Description of the *Interstellar Neutral H* Method

The principle of the *interstellar neutral H* Lyman α method is the following: the solar wind (and in minor proportions the solar EUV flux) is carving a cavity in the interstellar hydrogen flow distribution. The main solar wind effect is charge-exchange between the solar wind protons and the interstellar neutral H. Electrons play a negligible role. The shape of this cavity, deduced from the Lyman α resonance glow (scattering by the neutral H of the solar

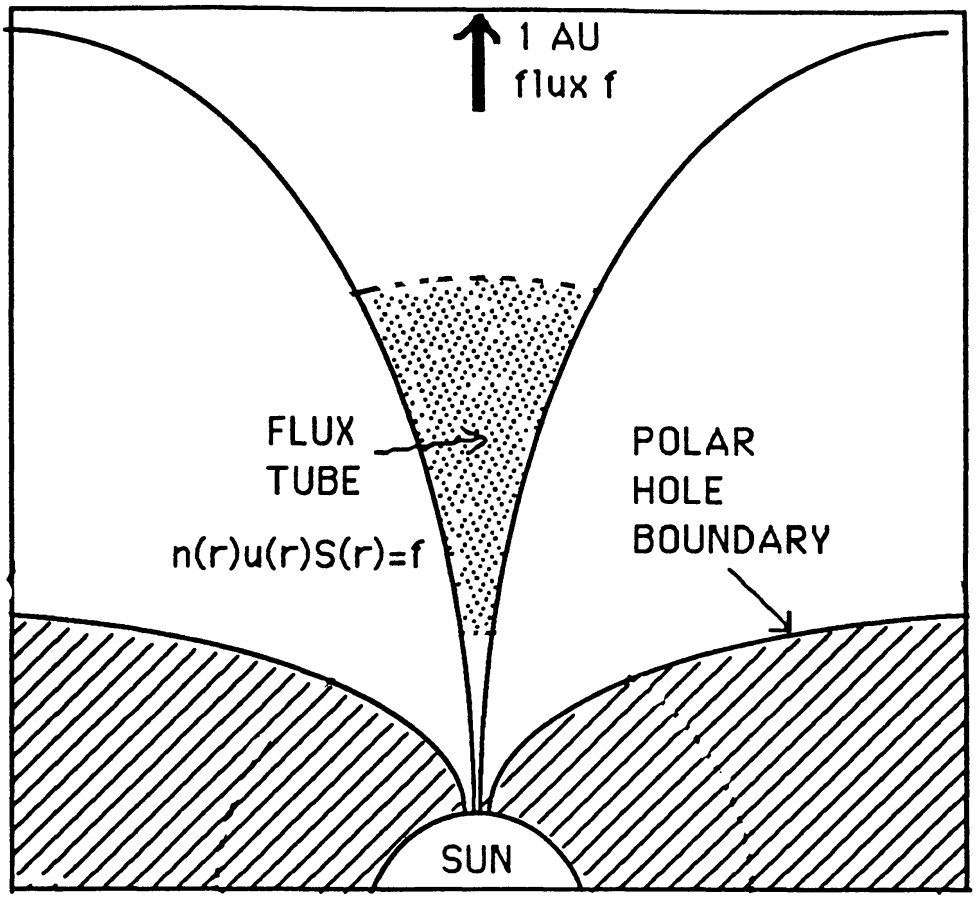

Fig. 1. This figure illustrates the expansion of the solar wind in a polar coronal hole. The solar wind flux ϕ at the pole can be measured by SWAN, whereas the LASCO coronograph can measure the electron density n and the surface area S. Therefore the velocity v can be derived, and the equation of dynamics can yield the kinetic temperature.

Lyman α photons at a rate of one photon every 500 s for one H atom at 1 AU) allows to infer the solar wind latitudinal dependence.

If the solar wind and EUV photon fluxes were isotropic, the H distribution would be axisymmetric around the Sun-wind axis (or upwind-downwind axis) as well as the Lyman α emission pattern. But this pattern is not axisymmetric, and the departures from axisymmetry reflect the properties of the solar wind encountered by the neutral H traveling at different latitudes (figure 2). The solar rotation averages the longitutidinal variations and mainly the latitudinal solar wind variations are inferred. The accurate determination of the solar asymmetries requires a mapping of the sky at Lyman α. Schematically, the near-ecliptic upwind-downwind variations are first fitted by a model with isotropic solar wind, then the departures from axisymmetry are fitted by introducing heliographic dependence of the ionization.

The characteristic scales of the phenomenon are the following: the size of the region contributing to most of the emission is about 5 AU on the upwind

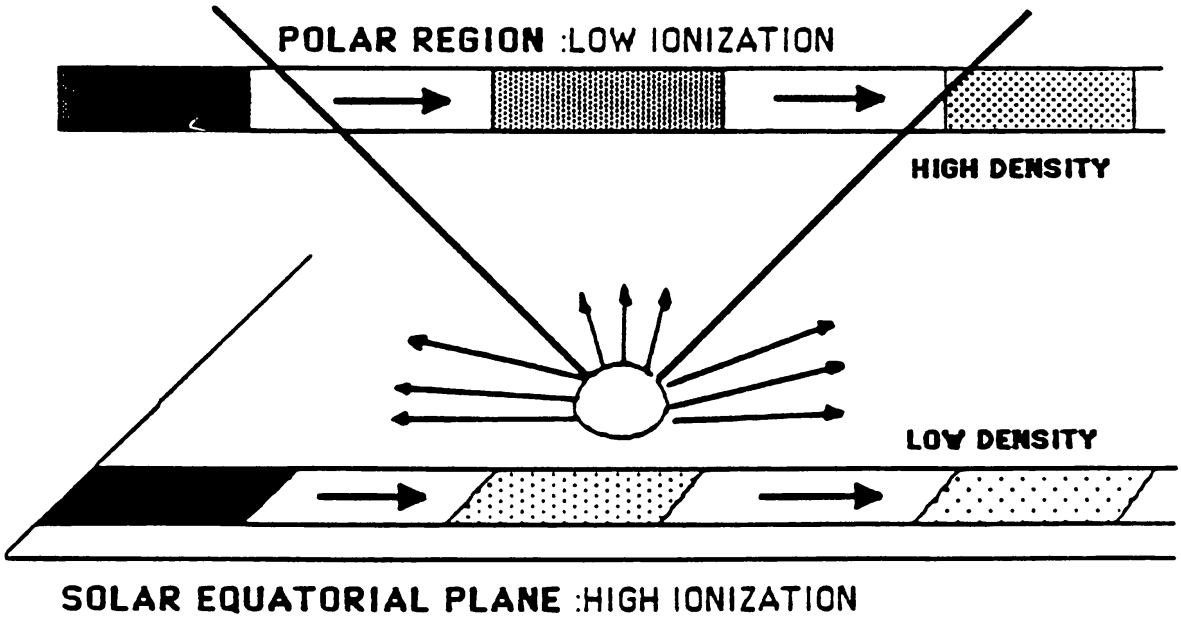

Fig. 2. Schematic illustration of the interaction between the hydrogen flow and an anisotropic solar wind, assumed to be smaller at high latitudes. The flow velocity is here assumed to be parallel to the solar equatorial plane for the sake of clarity. Atoms which travel near the solar equatorial plane do suffer higher loss processes by charge exchange with the solar wind than those atoms passing over polar regions (only the North hemisphere is represented here). Though the density difference increases along the flow vector, accurate modeling indicates that the effect of anisotropies are already detectable when looking upwind.

side (figure 5), 20 AU on the downwind side, and about 10 AU in the region where the departures from the isotropic (spherical solar wind) model are maximum. The latter direction is at 45° from the downwind axis and in a plane containing the pole and the wind axis (figure 4). The interstellar flow is moving at about 4 AU per year. The fact that the downwind region has been influenced by about three or even four years, twice more than the upwind side , shows that time-dependent models are necessary, if one wants to infer solar wind time variations with a temporal resolution finer than 2 or 3 years. A last important point is the difference between the influence of the solar wind and the solar photon flux. The former is a directional effect, i.e. H atoms at a latitude δ are ionized by solar wind issued from latitude δ. On the contrary, the same atoms are photoionized (and illuminated) by photons issued from the whole disk. This makes the photoionization much less latitude dependent as compared with the charge-exchange by the solar wind. Around solar minimum, the photoionization and the illumination are almost independent of latitude. At higher activity levels, this is no longer true, and one has to take into account latitude dependence of the photoionization and of the illuminating flux [Cook *et al.* , 1981; Pryor *et al.* , 1992; Ajello *et al.* , 1994].

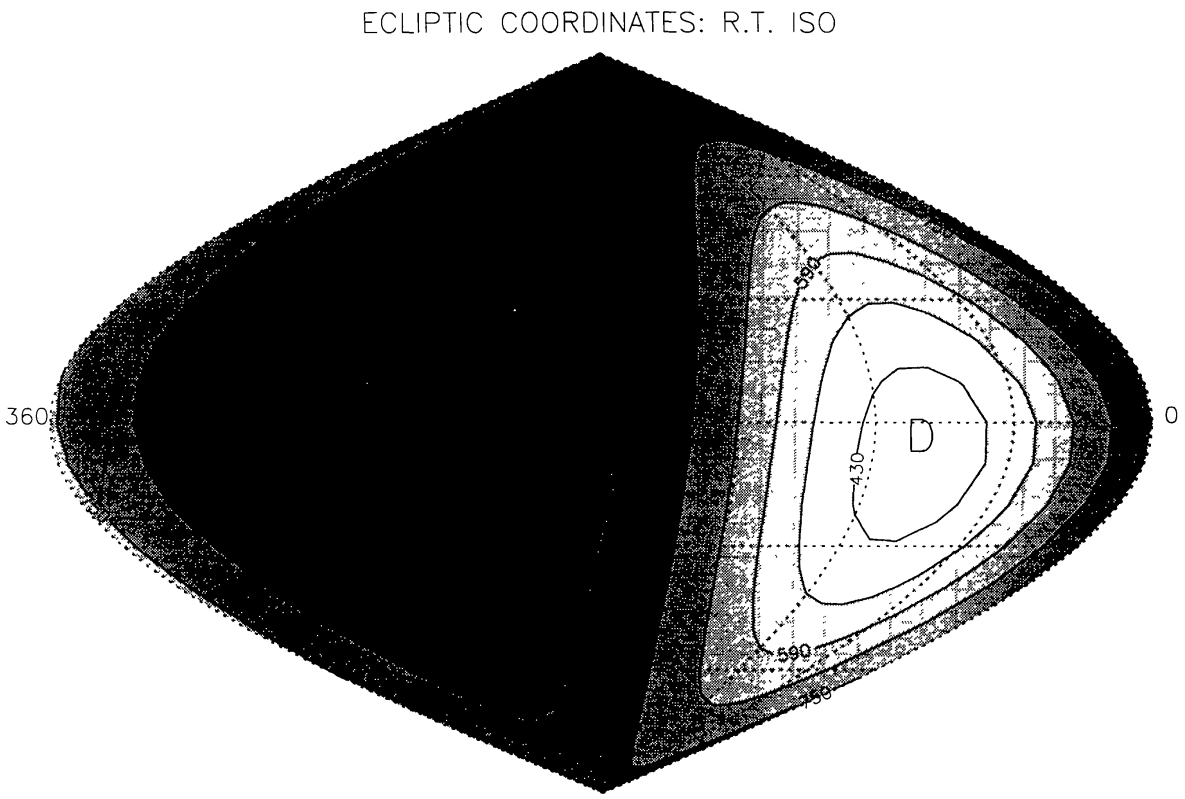

Fig. 3. Calculated isophote map of scattered interplanetary Lyman α for a spherically symmetric solar wind taking radiative transfer effects into account. Isophotes are labelled in Rayleigh. The model assumes $T_\infty = 8000$ K $V = 20$ km/s and $\mu = 1.0$. The H lifetime against ionization at 1 AU is equal to 1.2×10^6 s at 1 AU. The wind comes from ecliptic longitude 252°, ecliptic latitude 7.5° and is marked by letter U. The downwind direction is indicated by letter D.

The initial product of the H flow modeling and comparison with the data is the latitudinal variation of the global ionization rate of H (EUV photons $\lambda < 91.2$ nm + solar wind). After subtracting the ionization by solar photons we are left with the latitudinal variation of the pure solar wind ionizing power. Because the charge-exchange cross section decreases with the relative velocity of H and H^+, one has to use a model or a set of measurements describing the latitude dependence of the wind velocity, in order to derive the solar wind mass flux variation with latitude. Around solar minimum, the fast polar wind being a weaker ionizing agent as compared with the slow equatorial wind, the velocity field alone influences significantly the H distribution. With average velocities increasing from 350 up to 750 km/s, the charge-exchange cross section decreases by 32%. Only the remaining part of the observed ionization rate decrease is due to the mass flux variation.

Three remarks are in order at this point:

- The idea that solar wind asymmetries would impact on the Lyman α interplanetary (IP) radiation was first published by Joselyn and Holzer

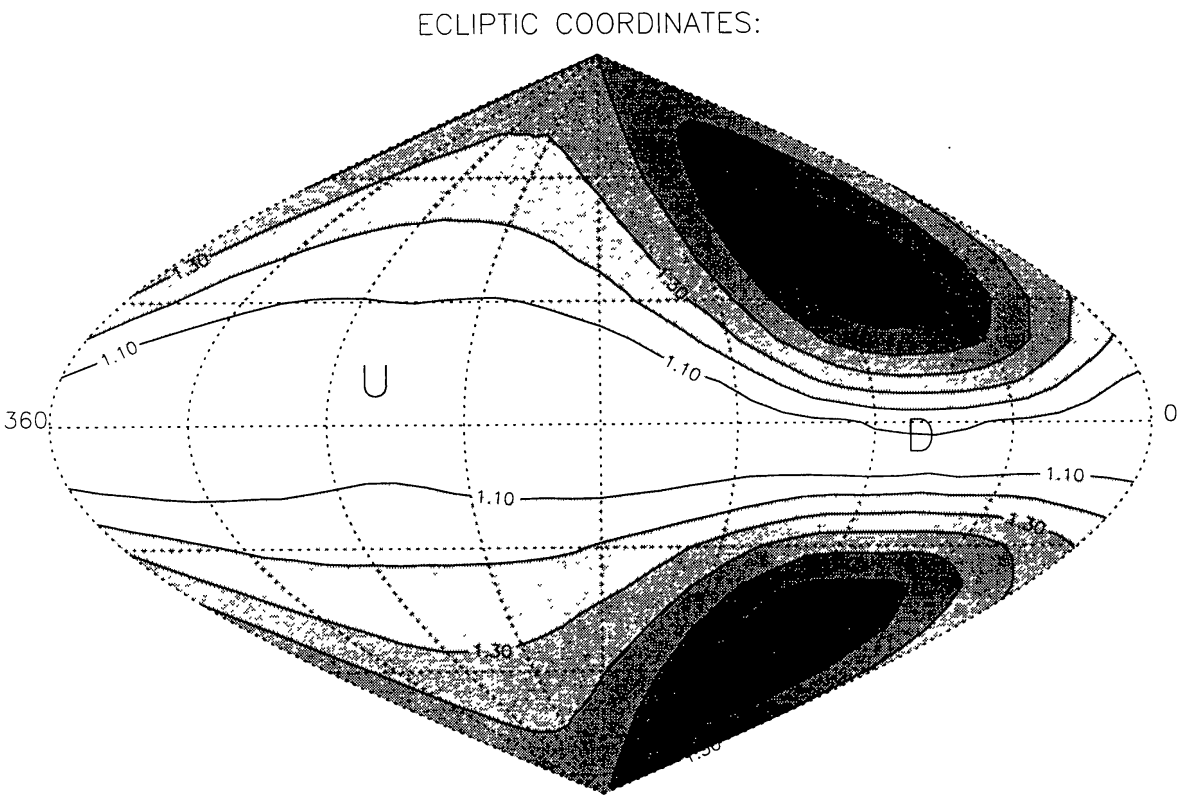

Fig. 4. The relative difference between maps with isotropic and non-isotropic solar wind is plotted as iso-contours every 10%. The increase from isotropic to non-isotropic solar wind is most intense in the median plane containing the downwind direction at 72° of ecliptic longitude. However the effect of anisotropy is already quite clear at the poles ($\approx$ + 25%)

[1975]. At this time, it was generally thought that the solar wind might be larger at the poles than in the ecliptic, at variance with later findings.

- During the charge-exchange process, the newly created neutral H escapes at $\approx$ 400 km/s and is no longer illuminated by the H Ly-α solar line because of the Doppler shift. As far as Lyman α emission is concerned, it disappears.

- The interstellar wind is flowing very near the ecliptic plane by pure chance. If it were flowing from a direction near the pole, solar wind variations would be almost impossible to detect.

2.3. Previous Results

Results obtained in the past from experiments on board Mariner 10, Prognoz 5-6, Voyager 1-2, and Pioneer-Venus have all shown a significant decrease of the total ionization of the neutral H from the ecliptic towards the solar poles, of the order of 20 to 40%. They have been all analysed by comparison with a stationary model: this means that for measurements done at a time t, the derived anisotropies refer to the 1 to 3 years period preceding the observations.

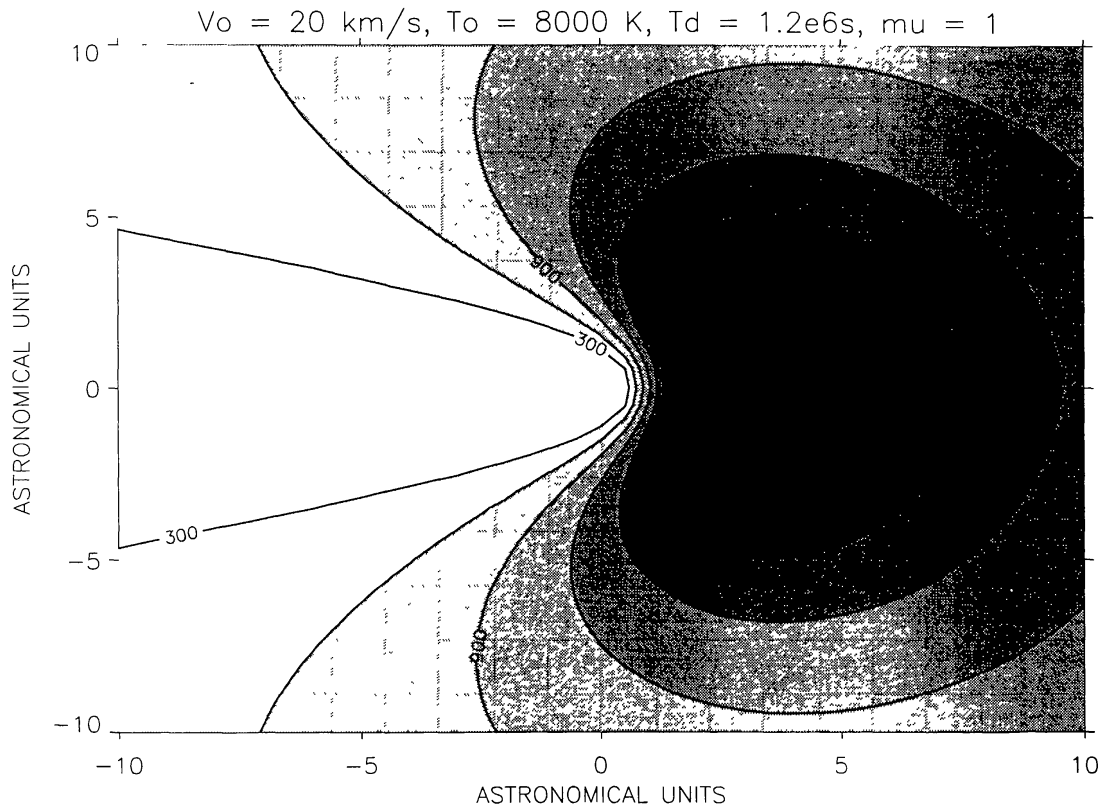

Fig. 5. Iso-emissivity contours of IP Lyman α. There is a strong maximum of emissivity located upwind from the sun at about 2.5 AU called the MER (Maximum Emissivity Region). Levels of iso-countours are in arbitrary units of the Lyman α emissivity (local production rate of photons). According to the changing SOHO position in the solar system, the MER region is observed in a variable celestial direction (parallax effect).

Because the photoionization is nearly isotropic (full disk average, in opposition to directional solar wind), the pole-equator decrease of the pure solar wind ionization is 5 to 10% larger, i.e. 25 to 50%. Then the knowledge of the latitudinal dependence of the wind velocity (up to now from IPS measurements, Kojima and Kakinuma [1987]) finally allows to derive the mass flux variations. However, in the context of the crude *harmonic* model (see below), contradictory results were obtained. The mass flux decrease has been found to be 25-30% in 1976-1977 [Lallement *et al.*, 1985], but only 0-10% in 1985-1986 [Lallement and Stewart, 1990]. This last result may be due to the inclination of the magnetic axis.

2.4. SWAN, LASCO AND UVCS

During the SOHO mission, the dynamics of the expansion of the fast solar wind in a polar coronal hole will be studied in the same fashion developed by Munro and Jackson [1977] and Lallement, Holzer and Munro [1986]. The LASCO coronagraph can yield both the contour of the coronal hole expansion volume (Figure 1), and the plasma density (electron scattering in the

corona). SWAN will yield the solar wind flux *at infinity* (say, 2 AU) as a boundary condition to the equations of dynamics, from which the temperature distribution in the corona may be derived. Needless to say that the additional informations from UVCS (temperature, proton density, velocity) will complement the diagnostic, in a search for a global consistency of the three data sets.

3. Forward Modeling and Inversion of Solar Wind / Lyman α Map

In this section we address the method of retrieval of the solar wind distribution from a Lyman α sky map. As explained above, the Lyman α sky map is sensitive to the latitude variation of the *ionization rate*, and this is what is retrieved. Then, assumptions about the solar wind velocity distribution must be made in order to derive the solar wind mass flux, because of the charge exchange $H+H^+$ cross section dependence on the velocity. During the SOHO mission however, we will be able to have an estimate from simultaneous extensive IPS campaigns.

3.1. Direct Inversion Retrieval

A typical interplanetary Lyman α map is characterized by a broad maximum emission region, with a minimum emission region in the opposite direction. It can be easily understood from the modeled distribution of emissivity (figure 6) that the maximum emission comes from the direction of arrival of the flow of interstellar wind H atoms, and accordingly this is how this direction was first determined from OGO-5 Lyman α maps [Bertaux and Blamont, 1971 ; Thomas and Krassa, 1971]. Most accurate values are now $\lambda_w = 252°$, $\beta_w = +7.5°$ in ecliptic coordinates [Bertaux *et al.* , 1985].

As a matter of fact, the celestial direction of the maximum emission depends also from the location of the observer in the solar system. Even from 1 AU from the sun, there is a significant parallax effect, with an angular displacement of the Lyman α maximum of $\approx$ 20-40°, when two maps are recorded at 6 months interval (for a 1 AU probe). This angular extent can be directly related to the distance of the maximum emissivity point and to the lifetime of one H atom versus ionization at 1 AU in the ecliptic plane (within the frame of some simplifying assumptions).

Finally, there are in the Lyman α data some relatively conspicuous departures from the axi-symmetry expected for an isotropic solar wind/ionization rate. Let us consider the Lyman α observations conducted with Prognoz 5 and 6, which recorded the Lyman α emission along a scan plane perpendicular to the Sun-Earth line at various positions in the solar system, described by their ecliptic longitude. Data and models are compared in figure 6 [Lallement *et al.* , 1985], corresponding to a near downwind position and a lateral

position. A big bump is observed around the North Ecliptic pole, a quite obvious departure from a model in which the ionization rate is isotropic (solid curve labeled A = 0). However, even in this very simple case, it is not possible to derive directly from the data the degree of anisotropy of the ionization rate distribution. We must compare the data to a series of computed emissions through *forward modeling* of various ionization latitudinal dependence, through a given H distribution. This early modeling of the H distribution by Blum and Fahr [1976] considered a monocinetic gas *at infinity*, whereas later models are using a full Maxwell-Boltzmann distribution at infinity : the so-called *hot* or thermal model [Lallement *et al.* , 1985].

3.2. Solar Wind Retrieval With Forward Modeling

For the analysis of both Mariner 10 [Kumar and Broadfoot, 1979] and Prognoz 5 and 6 instruments which recorded interplanetary Lyman α intensities [Lallement *et al.*, 1985], the latitudinal dependence of the ionization rate $\beta(\lambda, r)$ was first assumed to follow a harmonic function :

$$\beta(\lambda, r) = \beta_e \left(1 - A\sin^2\lambda\right) \frac{r_e^2}{r^2} \tag{1}$$

where β_e is the ionization rate at 1 AU (Astronomical unit), λ is the solar latitude, A is the anisotropy factor, r_e is 1 AU and r is the distance to the sun. This harmonic functional dependence has the great advantage that it can be integrated analytically along one H atom trajectory, alleviating the computation time of the forward modeling. In figure 6, the solid curve labeled A = 0.40 is such a harmonic model. The fit to the data is obviously much better than with an isotropic solar wind (A = 0), but it is not perfect.

Some progress was made more recently by the SWAN team in the field of retrieval. Summanen *et al.* [1993] considered a distribution of ionization rate defined for slices of 10° of latitude (still, symmetric about the solar equator) and re-analyzed the Prognoz data. A better fit was obtained with an ionization rate decreasing from 0° to ± 30° with large constant plateaus from ± 30° to ± 70°.

We wanted also to study the charge-exchange ionization rate caused by the solar wind. We used a model proposed by Zhao and Hundhausen [1983] for the latitude dependence of the solar wind velocity V.

The cross section for the charge exchange collisions as a function of V is calculated using the formula by Fite *et al.* [1962]. As a final result the solar wind proton mass flux was found to be as shown in 7 for various Prognoz observation. The flux is higher between ± 30° and there are large plateaus from ± 30° to ± 70°.

This overall behavior is strikingly confirmed by Ulysses *in situ* measurements, as displayed in 8. The mass flux measured by the SWOOPS instrument is shown as a function of the heliolatitude λ during the descent to

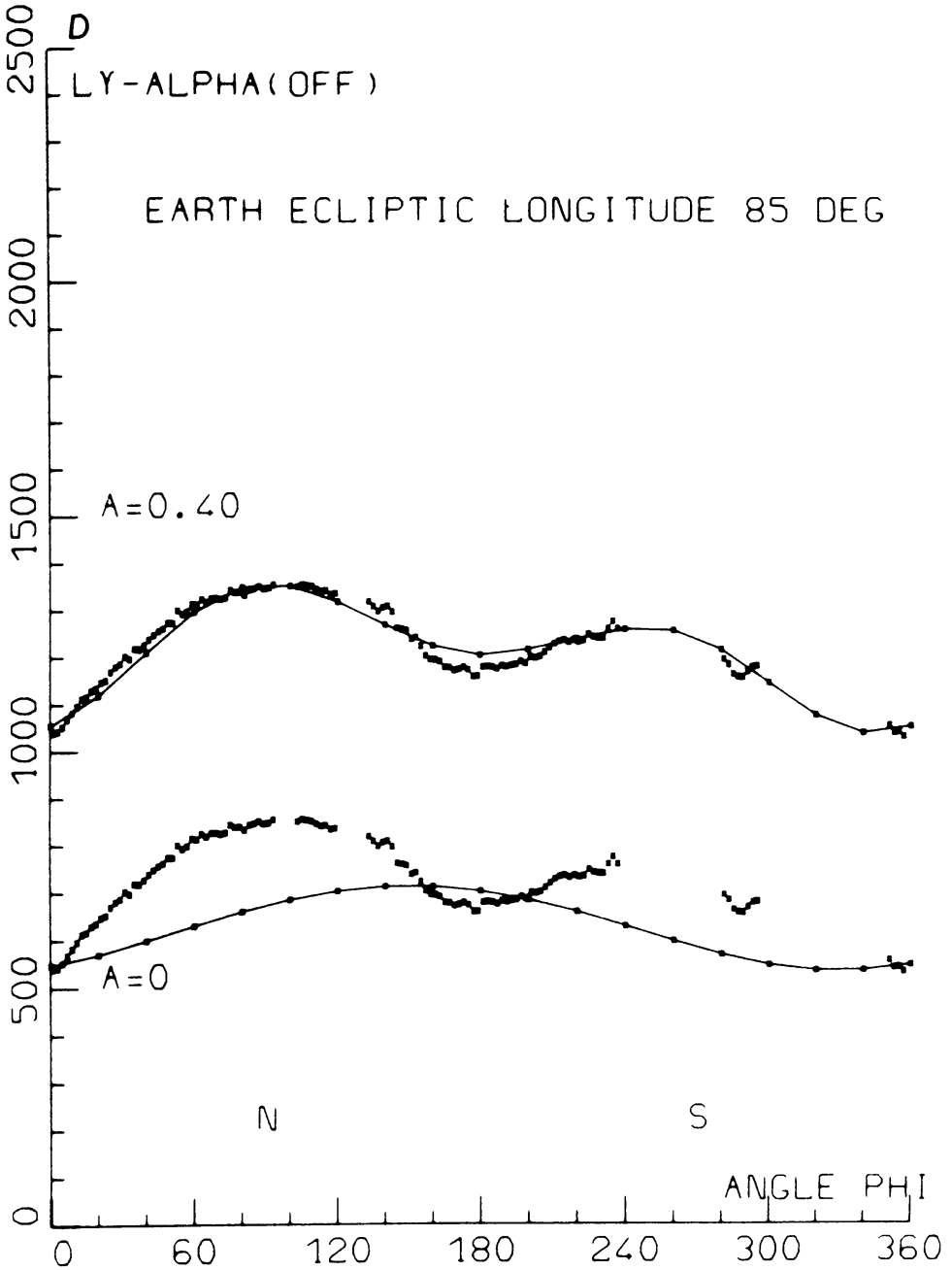

Fig. 6. Prognoz measurements of the interplanetary Lyman α emission (points) are represented as a function of spin angle f for the S4 observations at 85° ecliptic longitude and is compared to two different models of the solar wind effect. For the sake of clarity, data points are plotted twice. The ordinate scale in counts per second is valid for the lower set of data points compared to a model assuming an isotropic solar wind (A = 0). The same data points are displaced upward by 500 counts per second and are compared to a model including anisotropy of the solar wind characterized by the parameter A = 0.40. The north and south ecliptic directions are indicated by the letters N and S. The isotropic model shows only one maximum and one minimum, whereas both data and the anisotropic model show two maxima. In respect to the isotropic model the data points show more Lyman α emission toward the ecliptic pole, showing that the solar wind was less effective to destroy H atoms at high ecliptic latitudes.

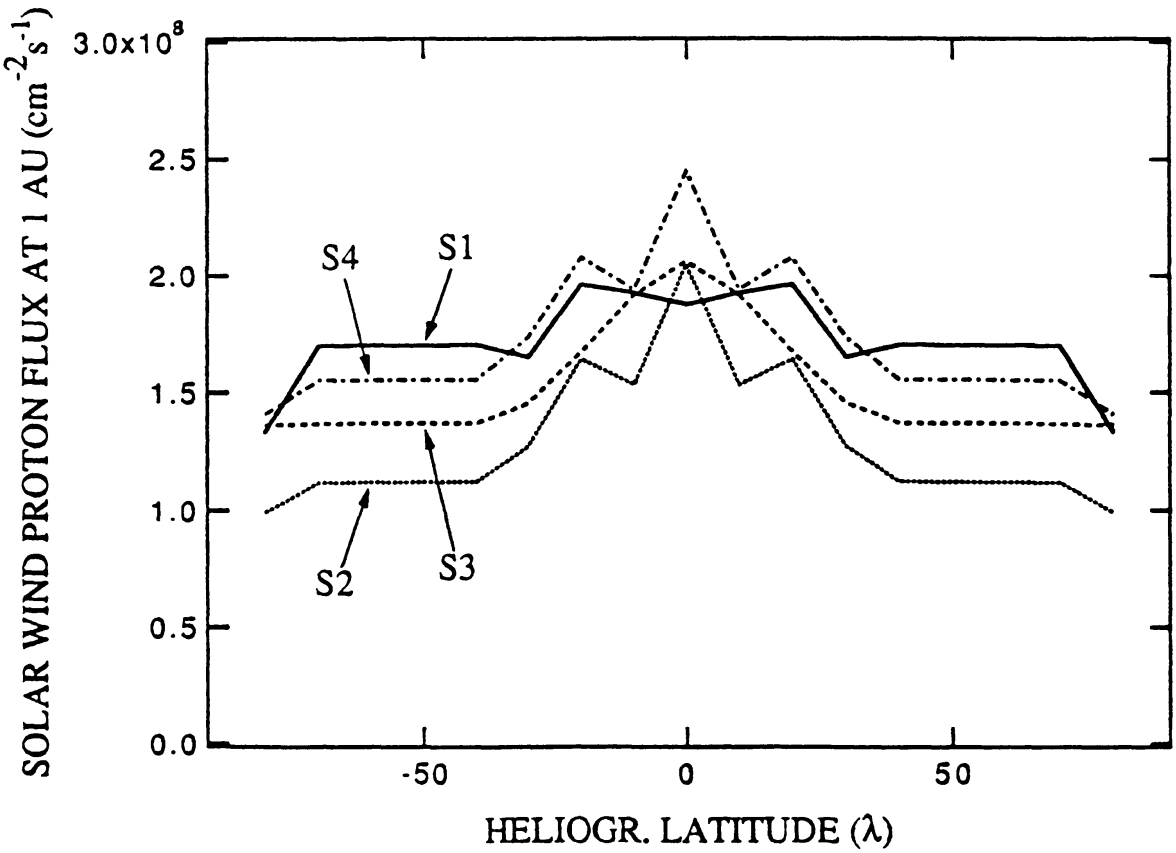

Fig. 7. Solar wind proton fluxes corresponding to ionization rates of the previous figure.

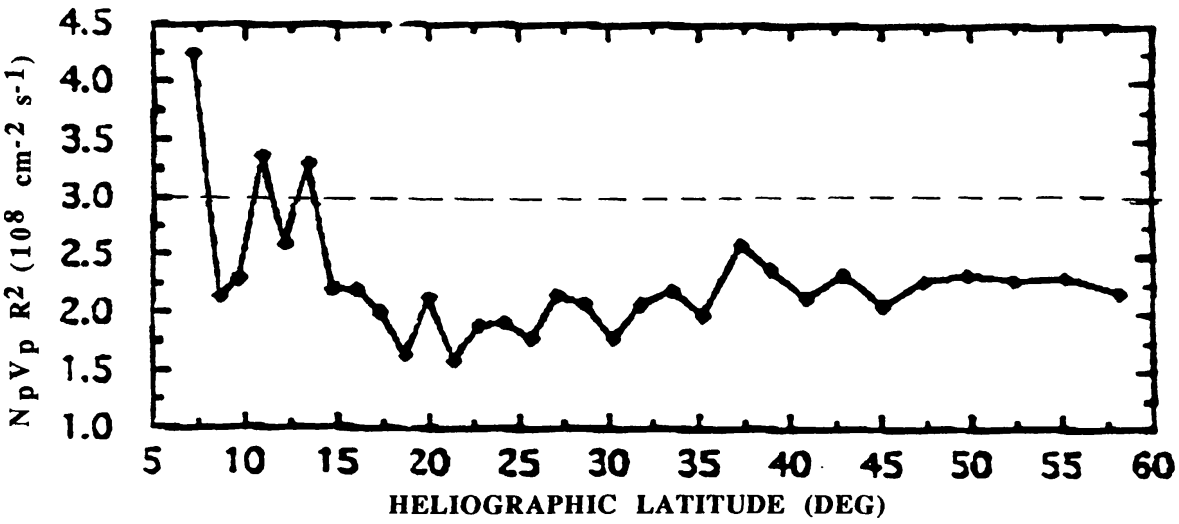

Fig. 8. Solar wind mass flux measured by the SWOOPS instrument as a function of the heliographic latitude on board the Ulysses probe. The dashed line at 3×10^8 cm^{-2} s^{-1} corresponds to the mean value of previous in situ measurements performed in the ecliptic plane for the past twenty years.

the solar south pole which began in 1992 [Phillips, private communication, 1994]. At λ smaller than 15°, there are strong variations which are associated to the curved neutral sheet, with maxima at the *normal* values (3.0-4.0 $\times 10^8$ cm^{-2} s^{-1}) currently measured in the ecliptic. Above 15° the mass flux is nearly constant with an average value of 2.0 $\times 10^8$ cm^{-2} s^{-1}, significantly smaller than the mean ecliptic flux. Assuming an identical behavior at positive latitudes, this implies an equatorial *ring* of large mass fluxes, and very broad *plateaus* characterized by a flux about 35-50% smaller. The main differences when comparing with the Prognoz results [Summanen et al., 1993] are the smaller latitude interval of the high flux equatorial region, and all the fluxes higher by a factor about 1.2-1.3, but the general shape is quite similar.

3.3. Lyman α Radiative Transfer

Up to now, for data interpretation the Lyman α radiation field has been most of the time computed within the frame of the optically thin approximation. However, in spite of the thin character of the H distribution near the sun ($\tau < 0.1$ per AU), it was found that radiative transfer effects are important, mainly because of the large asymmetry of the H distribution between the (relatively) high density of the upwind region and the low density of the downwind region [Quémerais and Bertaux, 1993].

Quémerais and Bertaux [1993] developed radiative transfer computer codes based on two different approaches giving the same results : one Monte Carlo approach and one numerical, iterative solution. As a result, they found indeed that all modelled Lyman α intensities seen from 1 AU are increased when multiple scattering is included, by a factor q varying from 1.03 to 1.30 with increasing angle of the line of sight with the upwind direction. The value of q is increasing strongly when approaching the downwind axis. Recalling figure 4 showing that the intensity increase due to latitude variation of solar wind is largest also in the downwind direction, it is clear that models of intensity must include radiative transfer for the interpretation of SWAN results. Up to now the approach of Quémerais and Bertaux [1993] was applied only to axisymmetric H distribution; the effect of a latitude variation of the ionization rate will have to be included, either trough a full 3-D radiative transfer code, or with a semi-empirical way to go from an axisymmetric solution (2.5 D) to a 3-D approximation. However, departures from axisymmetry of observed intensities are directly detectable (figure 6) without the use of highly sophisticated modeling, because the factor q depends mainly on the angle with the upwind direction.

3.4. Short Time Scale Variations of Solar Wind and Lyman α Emission

In this section we address the following question: is it possible to see on the Lyman α emission the effect of time variations of the solar wind, at time scales shorter than the solar cycle ? (the solar cycle is addressed in section 3.6). Here we will concentrate on the shortest time scales of ionization by the solar wind. Obviously, the nearer are the H atoms from the Sun, the faster the local density will react to an increase of the solar wind, and we will consider the upwind region, where there is a maximum of the emissivity (figure 5). A crude representation of the H density distribution $n(r)$ along the upwind axis can be found to be (exact for a monocinetic gas flow with stationary conditions):

$$n(r) = n_\infty \, e^{-r_c/r} \tag{2}$$

where n_∞ is the H density *at infinity* (before ionization is taking place), and r_c is the penetration depth of the H gas (the distance at which the density has been reduced by a factor e) given by :

$$r_c = \beta_o \frac{r_e^2}{v} \tag{3}$$

in which $r_e = 1$ AU, v is the incoming velocity of H atoms, and β_o is the ionization rate at 1 AU, assumed here to be isotropic (constant with latitude). Let the lifetime of one H atom being $T_D = \beta_o^{-1}$, and T_e the time spent by one H atom to travel along 1 AU:

$$\frac{r_c}{r_e} = \frac{T_e}{T_D} \tag{4}$$

which means that the penetration depth, expressed in AU, is equal to the ratio of the traveling time along one AU to the ionization time.

In the optically thin approximation, the distance r_{max} where the Lyman α emissivity is maximum (number of photon $\mathrm{cm}^{-3}\ \mathrm{s}^{-1}$) is obtained by multiplying the density distribution by r^{-2} (the Lyman α solar excitation rate), and finding r which gives zero for the derivative:

$$r_{max} = \frac{r_c}{2} \tag{5}$$

This point, placed upwind at $\approx r_{max}$ from the sun, is the center of the so-called Maximum Emissivity Region (MER). Obviously the intensity observed when looking at the MER is mainly due to the emissivity at this point, where the lifetime of one H atoms is:

$$T(r_{max}) = T_D \left(\frac{r_{max}}{r_e} \right)^2 = \frac{1}{4} \frac{T_e^2}{T_D} \tag{6}$$

TABLE II
IONIZATION/LYMAN α EMISSION REACTION TIMES

T_D : Lifetime of one H atom at 1 AU (second)	r_c (AU) : penetration depth	r_{max} (AU): distance of maximum emissivity	$T(r_{max})$: reaction time (days)
1×10^6	7.45	3.75	160
1.5×10^6	5	2.5	107
2×10^6	3.75	1.87	80
2.5×10^6	3	1.5	64

T_e has a fixed value of 87 days for $v = 20$ km/s. This formula shows a somewhat paradoxical result: the reaction time of the Lyman α emission to fast changes of the ionization rate, as measured by $T(r_{max})$, is inversely proportionnal to the lifetime of one H atom at 1 AU. In other words, fast variations of the solar wind are better reflected on the Lyman α emission when the solar wind flux has been small for a long time, because H atoms are penetrating nearer the sun and react faster. Table 2 indicate values for r_c, r_{max} and $T(r_{max})$ as a function of T_D for a typical range of its expected values as an illustration of formula (6).

These crude estimates are made with a series of simplification assumptions (stationary conditions), and a more sophisticated approach will be used when SWAN data will be analyzed. However, it shows that relatively short time scale variations of the solar wind ionization rate can be detected by monitoring the *upwind* Lyman α emission. Probably the 27 day variations, if any, would be smoothed out. On the contrary, the 1.3 year period of the solar wind velocity oscillations recently evidenced from IMP-8 and Voyager 2 spacecraft [Richardson *et al.* , 1994] with an amplitude of 100 km s^{-1} might be detectable in the SWAN Lyman α maps pattern. In particular, a possible latitude variation of this oscillation is an obvious target of interest to the SWAN investigation.

Not only short time scales can be observed more easily when looking upwind in the direction of the MER; small scale features of the solar wind latitude variation could also be observed better when looking upwind. On the Prognoz data obtained in a plane perpendicular to the ecliptic and scanning vertically through the MER, a pronounced dip of about 10% in the intensity was found near the ecliptic with a width of $\approx 30°$ of latitude. This is the clear signature of a peak in the ionization rate as a function of latitude, concentrated near the ecliptic plane. This unique observation of February 1977 is likely related to a time near the solar minimum when the neutral

sheet of the solar wind was very flat, and not warped as usual. Therefore, during the solar rotation the neutral sheet is sweeping across the MER, but staying in the heliographic equatorial plane.

3.5. Anisotropies of the Solar Lyman α Irradiance

A correct modeling of a Lyman α map includes the source of Lyman α photons: the Sun. The time of SOHO launch is the beginning of a solar minimum period, and accordingly we do not expect important departures of the solar Lyman α irradiance from spherical symmetry. However, we must be ready to account for even minor departures. Longitudinal variations will reflect on the SWAN Lyman α maps where *bulges* connected to active solar regions will drift with the 26 days period.

For latitudinal variations, we will rely on two other data sets. First, apparently there is a good correlation between the line width of the Fraunhofer Helium line at 1083 nm and the total solar Lyman α line [Ajello *et al.* , 1994]. However, it is not yet proven that the correlation is the same for the *center* of the solar Lyman α line, which excites the resonance of interplanetary H atoms. SUMER observations could be used to establish such a correlation, which can be made either at the level of the integrated disc, (time correlation), or on individual areas of the Sun where both the Lyman α solar spectral profile and groundbased 1083 nm observations are performed. One full map of the whole disc performed by SUMER team could be sufficient for this purpose. It is well known that both the intensity and the line profile of the solar Lyman α line changes from quiet areas to active regions. From such SUMER maps, we could reconstruct the solar irradiance field, both in longitude and latitude.

3.6. Solar Cycle Modulation of the H Density Distribution

Up to now the modeling of the H density distribution was assumed to be stationnary as developed for instance by Lallement *et al.* [1985]. However, the UV radiation flux has a strong solar cycle variation. The solar Lyman α can have 60% modulation during the solar cycle. The ionization part of the radiation field is estimated to have up to a factor of three variations. The solar wind also varies according to solar cycle, resulting in up to a factor of two variations of the ionization rate in the ecliptic plane.

Hydrogen atom trajectories are determined by a central force which is a sum of the gravitational force and the radiation pressure force. For hydrogen these two opposite forces are near balance but during the solar cycle the net force does show both attractive and repulsive phases. As a consequence hydrogen atom trajectories tend generally to be a mixture of repulsive and attractive trajectories [see Kyrölä *et al.* , 1994]. Not only individual trajectories but the whole ensuing density distribution will be modified by the solar cycle. The solar cycle modifications in the density distribution are most

clearly seen when the temperature of the flowing gas is low. It has been shown [Blum *et al.* , 1993; Kyrölä *et al.* , 1994; Bzowski and Rucinski, 1995] that a time dependent central force gives rise to a constant succession of depletion areas and focusing peaks downwind from the Sun. These structures travel at the bulk velocity of the incoming gas. How much they affect the measured quantities, i.e. Lyman α intensity and line shape is still under investigation. Models which also include time dependent latitudinal changes and the temporal modifications of the terminal shock position are also candidates for development by the SWAN team or their colleague scientists.

4. Description of the SWAN Instrument

4.1. Overview and Electronic Unit

In order to provide a full sky map from the 3 axis stabilized SOHO platform, SWAN is composed of two identical Sensor Units (SU); one is mounted on the +Z body axis of SOHO and allows to map slightly more than one hemisphere centered on +Z, while the second one is mounted on the -Z face. Because of the attitude control of SOHO, which maintains +X towards the center of the Sun, and the solar rotation axis in the plane XZ, the +Z axis is near the North Ecliptic pole (similarly the -Z axis is nearly the South Ecliptic pole), but not in a fixed celestial direction along the year.

The instantaneous field of view of one sensor unit is a square of $5 \times 5°$ divided in 5×5 pixels of $1°$ square each. The central line of sight can be oriented toward any point of one hemisphere by a mechanical periscope system containing two mirrors at $45°$ incidence. While this system is oriented and maintained toward a specific position, UV photons are counted in each pixel of the detector for a typical duration of 45 seconds. A motion of one or two of the mechanisms is then activated to measure the intensity distribution in another FOV of $5 \times 5°$. Covering the whole sky with a $1°$ resolution can therefore be accomplished in less than one day.

In addition to this purely photometric mode, one hydrogen cell placed in the optical path can be activated to yield a quantitative information on the spectral profile of the Lyman α line, with a resolving power of $\approx 3 \times 10^5$. One Electronic Unit (EU), mounted on the Payload Module on face -Z, contains a redundant microprocessor to control both sensor units and provides the electrical interface to the spacecraft. The design of the microprocessor unit is based on radiation tolerant 80C86 architecture. The control of the sensor units by a microprocessor enables various measuring modes, as well as self-monitoring functions, to be accomplished easily by software. All communications to the Earth is carried out via the spacecraft telemetry and telecommand system. The interface to the spacecraft telemetry system is for downloading the measurement results to the Earth. The interface to the spacecraft telecommand system is for selecting the measurement mode and

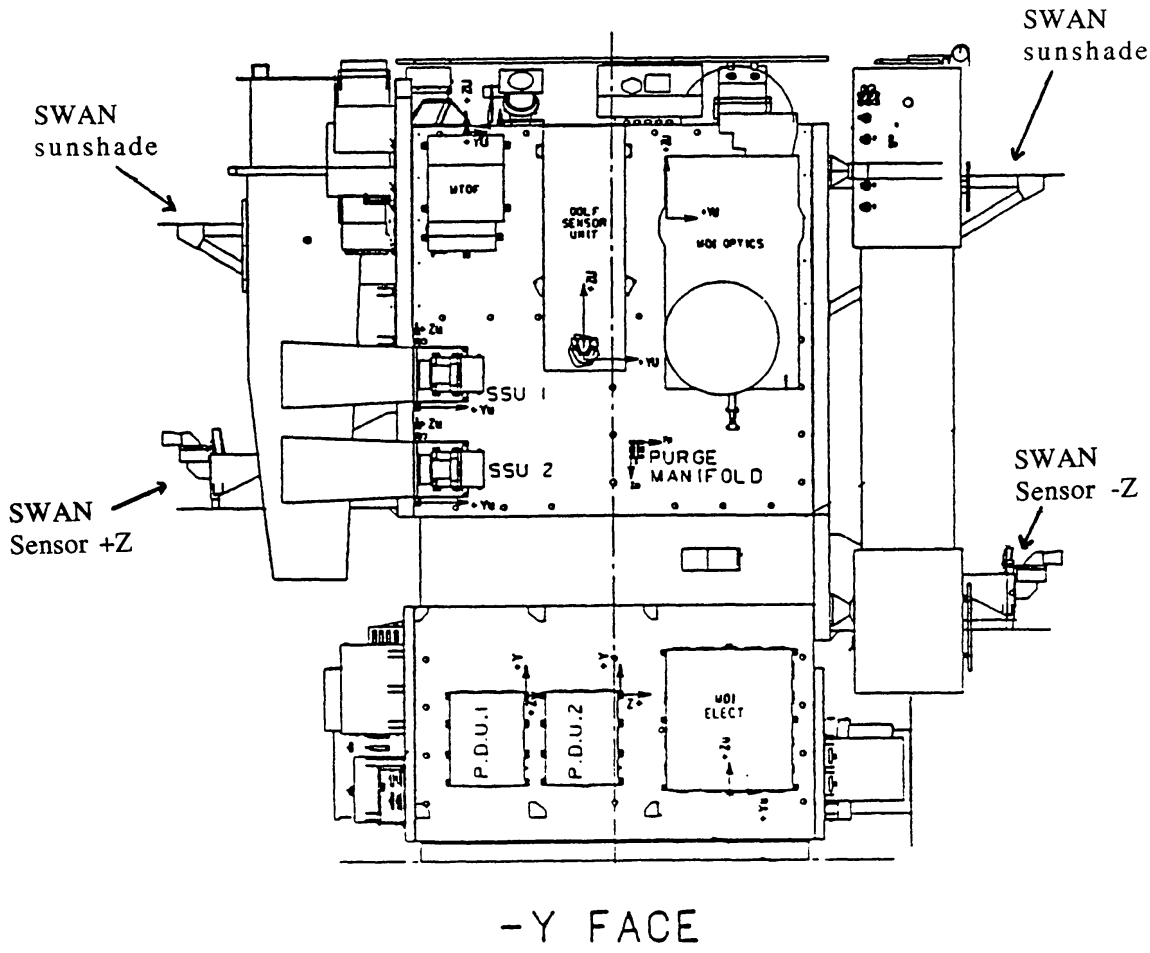

Fig. 9. Accomodation of the two SWAN sensor units on the SOHO spacecraft Payload Module. Each of them allows to make a map of a whole hemisphere. A sun shade protects the entrance of the instrument baffle.

for controlling some parts of the instrument electronics. The redundancy is based on an unpowered spare microprocessorunit that can replace the active unit by telecommands sent from the Earth via the instrument spacecraft interface. There is the possibility to modify the internal software by telecommand.

4.2. Accomodation

Each Sensor Unit is mechanically mounted on a pedestal which protrudes somewhat from the sides of the SOHO Payload Module (figure 9). A sun shade, also mounted on the same side, prevents the solar light from shining on the entrance of the mechanical baffle, whatever is the position of the periscope, thus allowing to obtain good observations in the solar hemisphere, at very low angles to the Sun. This sun shade should allow to observe the coronal Lyman α emission down to a distance of about 10 R_S(solar radii), which is the outer limit of UVCS measurements.

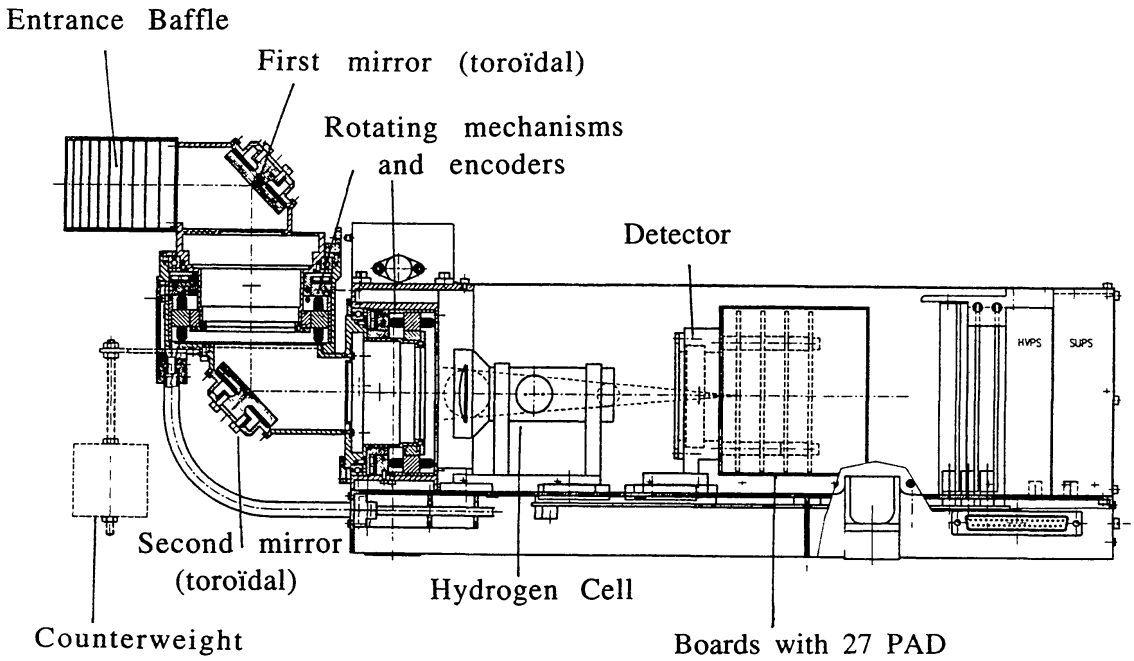

Fig. 10. Optical configuration of one Sensor Unit.

The observation of some portions of the sky should be precluded by some SOHO appendages (Solar panels, thrust nozzles), but these limitations have been minimized as much as possible by careful implementation of the Sensor Units. Another specific appendage has been implemented by SOHO project in order to protect SWAN from hot gas firings, when the thrust nozzles are used.

4.3. Optical System of One Sensor Unit

4.3.1. The Periscope System

In order for each SWAN sensor unit to be able to scan a half sky (2π steradians), a periscopic mechanism including two 45° incidence mirrors with orthogonal rotation axis has been developed (see figure 10). The rotation range for each mirror is $\pm$ 130° around its central position, with an accuracy around 0.1° to allow sub-pixel calibration [Huomo *et al.* , 1992]. Each rotating mechanism is driven by a 90 poles Sagem (F) 35PP81 stepper motor used in micro stepping mode with a maximum torque of 0.4 Nm.

The rotor and the stator are assembled with a Kaydon (USA) preloaded 4 point ball bearing with MoS_2 coating. During the launch phase the mechanisms are prevented to rotate by a pin puller mechanism developed by Starsys Research (USA) and the axial deflexion is reduced by the use of heavy preloaded (400 N) bearings. The environmental test campaign showed that the friction torque of such a mechanism increases at low temperatures

and get stuck. This lead to the addition of a one Watt operation heater on the outermost mechanism to maintain its temperature above 0° C. The operating temperature range of the mechanism is now -10 to +40° C with at least 50% torque margin, whereas a thermal model predicts an equilibrium temperature of +6° to +17°C.

The position of each mechanism is given by a cylindrical shaped Penny and Giles (UK) potentiometric encoder and transmitted each 15 seconds in the instrument telemetry. The power for the outer mechanism and its encoder information is routed through a mobile harness to allow the inner mirror rotation. These Teflon wires are wrapped in a spiral cut Teflon tubing surrounded by a gold coated copper-beryllium spring to prevent tangling during launch vibrations.

The total weight of this two axis mechanism is 2200 g and the power consumption during one motor motion is 2.2 Watt.

4.3.2. Optical Configuration

As said above, the two Sensor Units are identical. The optical system of each SU (figure 10) is composed of two concave mirrors of torodial shape, mounted in the steerable periscope. This system of mirrors produces a map of the field of view on the entrance window of the H cell which is a MgF_2 lens. The exit window of the H cell refocuses the beam on the cathode of the UV detector, placed some 48 mm (TBC) behind the cell.

This optical scheme deviates significantly from the original one considered at the time of the proposal. At this time, the two mirrors were plane, and the detector was placed just behind the H cell, whose MgF_2 entrance lens focussed the beam to obtain an image of the sky on the entrance of the detector. In such a scheme, the unobstructed FOV seen from the MgF_2 lens, which was the entrance pupil, required a relatively large entrance baffle. As a result, the thermal escape to empty space was rather severe, and the expected low temperature of the periscope mechanisms was a problem for the ball bearings. The final design with torodal mirrors allows for a much smaller entrance diameter $\approx$ 27 mm of the baffle and a corresponding smaller thermal escape. Another advantage is that the detector is furthered from the H cell, which filaments might a have been a source of stray light when heated electrically. A price to pay for this solution is a somewhat degraded image quality. However, the radii of torodal mirrors were optimized through ray tracing computations, which shows that one parallel beam of light gives a spot size always smaller than one square pixel of $1 \times 1°$ (typically $0.3 \times 0.3°$, figure 12).

4.3.3. Spectral Efficiency

Built from Aluminum, the mirrors are coated with an Al + MgF_2 coating, providing at Lyman α wavelength a reflective efficiency of $\approx$ 77% at 45° incidence, relatively insensitive to air humidity on the long term.

The MgF_2 lenses of the H cell are made of high UV quality MgF_2 crystals (Sorem, France), polished to the required spherical surfaces. The combined Lyman α transmission of the two lenses, once the cell is completed, was measured in the range 18-30%, depending on the specific unit. The MCP detctor includes a 5 mm thick MgF_2 entrance flat window, and a semi-transparent CsI photocathode, so-called *solar blind* for its cut-off efficiency above $\approx$ 200 nm. According to the vendor (Hamamatsu) the quantum efficiency of the detector is $\approx$ 8-10% at Lyman α, depending on the unit.

One can get an idea of the overall spectral efficiency (relative) by looking at figure 11, which represents the counting rate of one sensor unit as a function of wavelength, when illuminated by synchrotron radiation with a relatively flat spectrum through a monochromator. The main features of this curve are: the short λ cut-off wavelength at 115 nm provided by MgF_2 material, the long λ cut-off at $\approx$ 190 nm provided by the CsI cathode, and some strong absorption features caused by the presence of residual gaseous HCl contained inside the H cell.

In order to reject the light of UV stars, we had considered the possible addition of one optical filter, isolating a bandwidth of $\approx$ 10 nm around Lyman α, as implemented in our earlier-Prognoz experiment. Such an optical filter (a thin film deposited on a MgF_2 window) unfortunately has a peak transmission of only 15%. A simulation of the stray stellar signal over the whole sky divided in $1 \times 1°$ pixels was performed with the 5200 brightest stars of the Bright Star Catalogue, taking into account the spectral efficiency of SWAN without any filter. Only 173 pixels are contaminated with a signal larger than 10 count/s, out of 41242 square degrees of the whole celestial sphere [Berthé, 1995].

By putting a Lyman α filter of 10 nm width, the contamination by stars cooler than $\approx$ A_3 spectral type would have been eliminated completely. Still, hotter stars would have been seen also, their continuum contributing to the bandwidth 121 $\pm$ 5 nm. However, the major part of the sky is not contaminated by stars, even without a filter. It was estimated that the gain of suppressing the contamination on $\approx$ 1% of the sky was not compensating the loss of sensitivity at Lyman α by a factor of 6 that would have resulted from the addition of the Lyman α filter, and such a filter was not implemented finally.

One of the detector pixel is covered with a BaF_2 window, which short wavelength cut-off is $\approx$ 140 nm. A sky map with this pixel will allow to measure the stellar contamination above this wavelength, as well as some diffuse

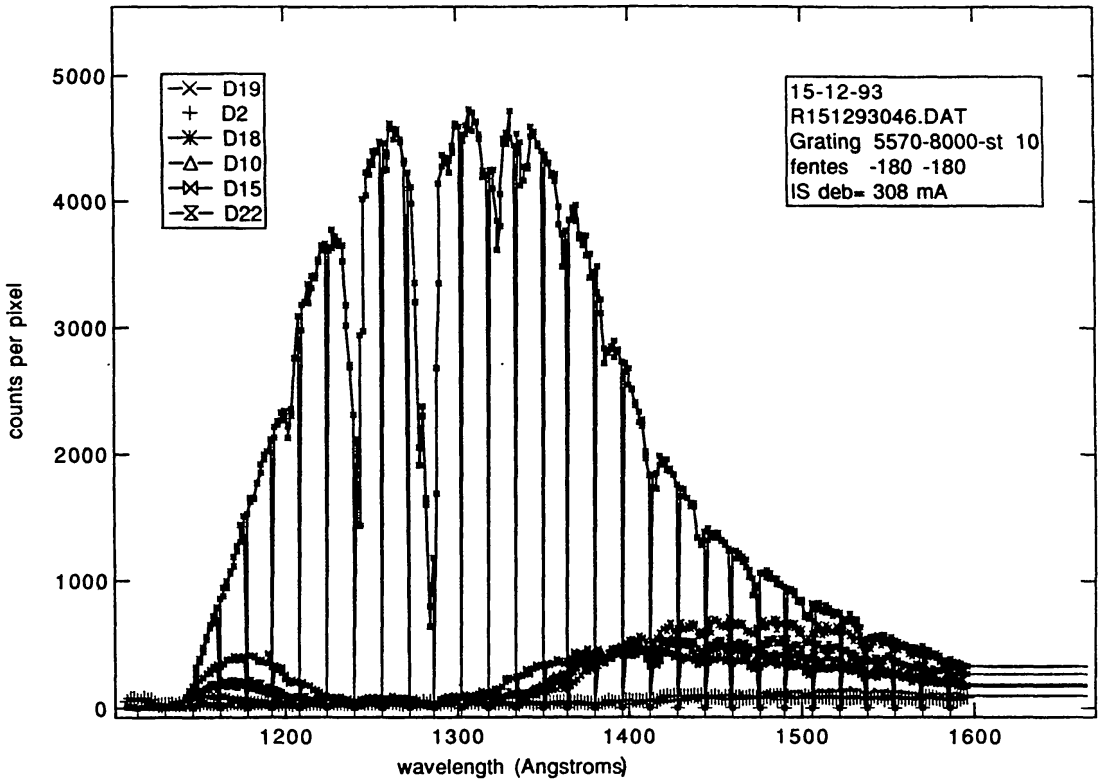

Fig. 11. Counting rate of one SWAN Sensor Unit when exposed to a monochromatic beam of light generated by synchrotron radiation, for 6 different pixels. Several troughs are due to HCl absorption present in the hydrogen cell. The beam is well focused by the MgF_2 lenses of the cell on one single pixel for a wavelength of $\approx$ 124 nm.

emission observed recently in the region of the galactic center [Quémerais *et al.* ,1995].

Chromatic aberration. The index of refraction of MgF_2 is rapidly changing with λ in the far UV around Lyman α. As a result, all wavelengths cannot be focussed together on the detector: around 120 nm, the small image of synchrotron radiation is fully contained in one detector pixel, whereas for shorter and longer wavelengths, some adjacent pixels are also illuminated. The image of a star will usually not be contained on a single pixel. The equivalent focal length of the optical system is $\approx$ 102 mm at Lyman α.

4.3.4. Multi-Anode Detector

The detector is a Multi-anode MCP detector tube from Hamamatsu. The front window is a thick MgF_2 flat window, of 25 mm diameter. The semi-transparent Cesium Iodide (CsI) cathode is deposited on the inside of the front window. A micro-channel plate multiplier containing two stacks multiplies the photo-electron entering the microchannel plate tube, and the total corresponding charge at the output of the MCP is collected on a set of several square anodes. Each of them is a square of 1.78 $\times$ 1.78 mm, corre-

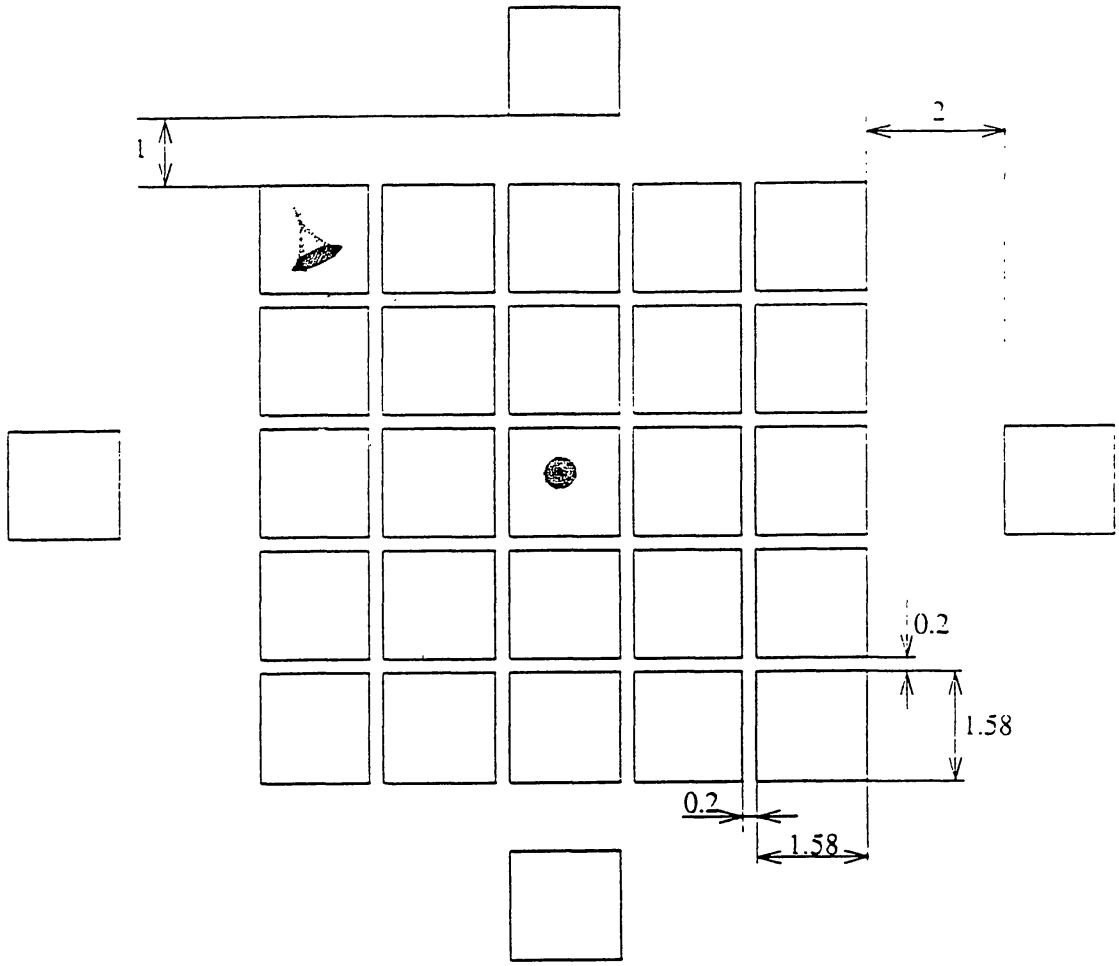

Fig. 12. Physical configuration of SWAN detector pixels. Sizes are in mm. Each pixel covers 1 x 1° on the sky. Side pixels are used for Dark current counting. On one of the sensor unit, the bottom pixel is covered with a BaF_2 filter which blocks all radiation below 1400 Å. In some pixels are represented the image of a monochromatic source at Lyman α computed from ray tracing.

sponding to 1° × 1° for the equivalent focal length. The various anodes are positionned as presented in figure 12, according to a custom made design for SWAN purpose. Out of the 29 anodes, only 27 are connected individually to 27 pulse amplifier/discriminator (PAD), which deliver pulses to 27 counters. Only a fraction ρ_c of all pulses generated by photo-electrons are delivering a pulse counted in the counter; indeed the charge inside one pulse must be larger than the PAD threshold of $5 \times 10^4 e$. The pulse-height distribution is a function of the MCP gain controlled by High Voltage across the MCP, which can be varied from a ground command to the HVPS. Therefore, the value of ρ_c depends on the HV level. Actually, ground calibrations indicate that on most SWAN detectors the counting efficiency is below 50%, even at the highest level 2400 V recommended by Hamamatsu.

It is well known that for a given HV level the gain of a MCP stack depends on the total charge which was extracted from the MCP. Therefore, one must find a compromise between running the MCP at a very high voltage level to improve the statistics by increasing ρ_c and the number of counts, at the expense of a shorter lifetime of the detector, or applying the opposite strategy [Berthé, Ph.D. Thesis, 1995].

It should be noted that the first detector was bought from ITT. Though its performances were satisfactory, we were obliged to switch to Hamamatsu when ITT cancelled in 1991 its production line of scientific detectors. Hamamatsu built the detector according to our design, in which all 25 pixels corresponding to the 5×5 square blocks are connected to a PAD /counter chain; two additionnal ones, on the sides, are in principle supposed to give an estimate of the Dark count rate, because they are placed outside the Lyman α FOV. However, because of spherical aberrations they are sensitive to stellar light of other wavelengths. In one of the Sensor Unit, a BaF_2 filter has been glued to the MgF_2 entrance window, in front of the bottom pixel of figure 12.

A scanning of the small image of synchrotron radiation output, through a monochromator at 40 meters from the sensor unit, is displayed in figure 13, showing the sharpness of the pixels response to a parallel beam of radiation.

4.3.5. The Hydrogen Absorption Cell

The pyrex vessel with its two MgF_2 lens windows is represented in figure 14. The internal distance between the windows is 76 mm (CK). The cell is sealed and permanently filled with H_2 gas at few hundreds of Pascals pressure. Two tungsten filaments can be independently heated electrically, and H_2 molecules touching the filament are dissociated into atoms, creating an optical absorption of atomic hydrogen Lyman α line. When the filament is switched off, there is immediate (within 0.05 s) recombination into molecules. Whereas H_2 is totally transparent to Lyman α, when the hydrogen atoms are created inside the cell, incoming photons lying near the resonance line center are absorbed and scattered on the cell walls where they disapear. The measured transmission function of the cell is represented in figure 15 as a function of $\nu = \frac{c}{\lambda_o}(\lambda - \lambda_o)$, λ_o being the resonance Lyman α line wavelength ($\lambda_o = 121.566$ nm). It is shown that for a typical working level, the H cell acts as a *negative filter*, blocking every photon lying within $\approx \pm 20$ mÅ (or 5 km/s doppler shift) from λ_o.

Because the interstellar hydrogen is flowing through the solar system at the velocity of about 20 km/s and the SOHO spacecraft is moving around the sun at the velocity of about 30 km/s with a direction varying as a function of the time of the year, the relative velocity V_r between SOHO and the interstellar gas varies from 10 to 50 km/s. Therefore the scattered Lyman α

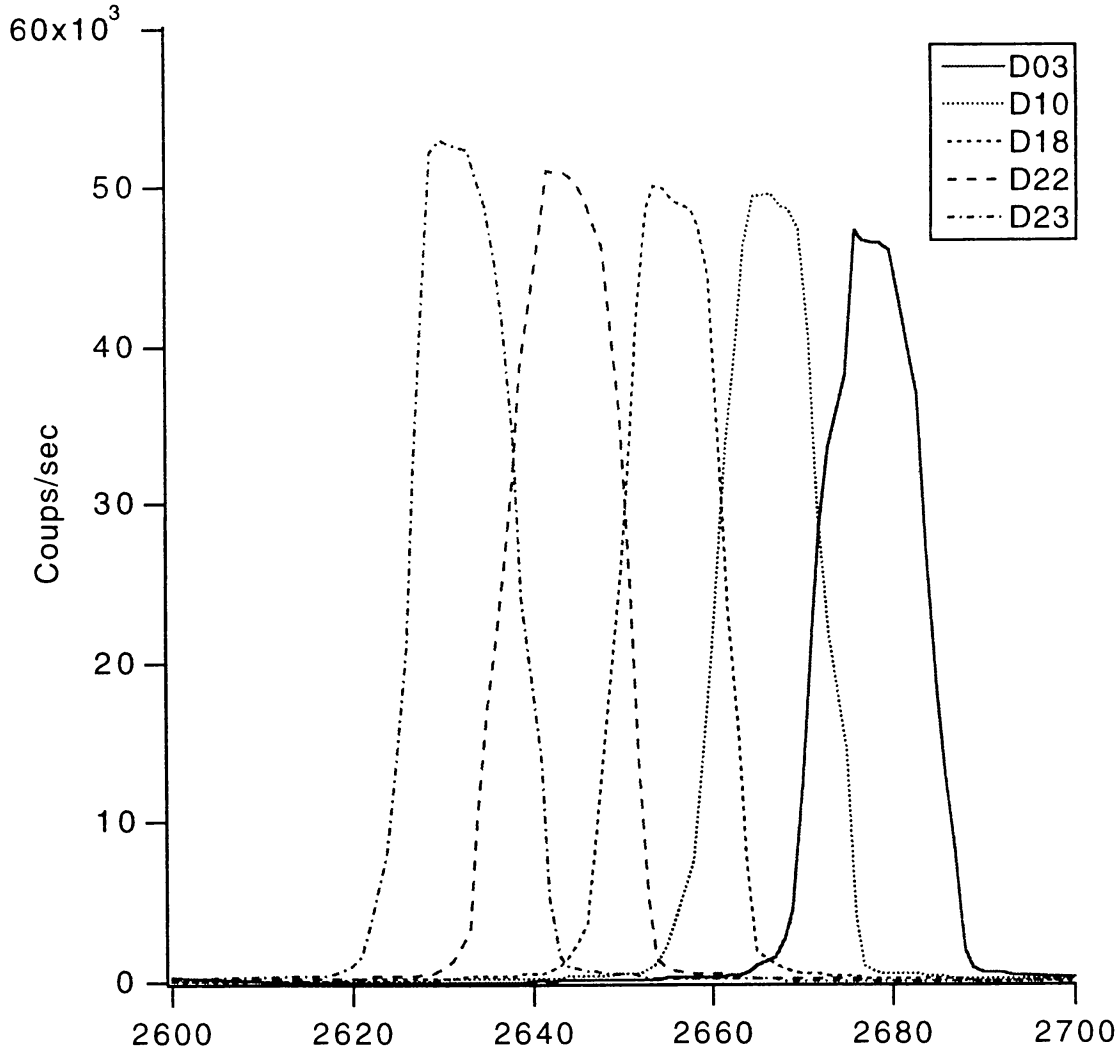

Fig. 13. Response of various pixels on a line, when the image of a synchrotron radiation monochromatic spot is moved across the detector with the periscope mechanism motion. The horizontal scale represents step of 0.1°.

light will have a Doppler shift which depends on both the time of year and the direction of sight.

When the cell is OFF, the total Lyman α radiation is measured by the detector. When the cell is ON, only the fraction outside the *negative filter* is measured (figure 15). The ratio of the intensities $R = I_{ON}/I_{OFF}$ is called the reduction factor, and is measured by sequentially switching the cell on and off while looking at the same sky direction.

Depending on the radial velocity of the absorption cell and interstellar gas the interplanetary emission profile will shift relative to absorption profile in the H cell and the detector signal changes as seen in figure 16. The Doppler shift is always zero when looking perpendicular to the relative velocity vector and the reduction factor is minimum in that direction because the absorp-

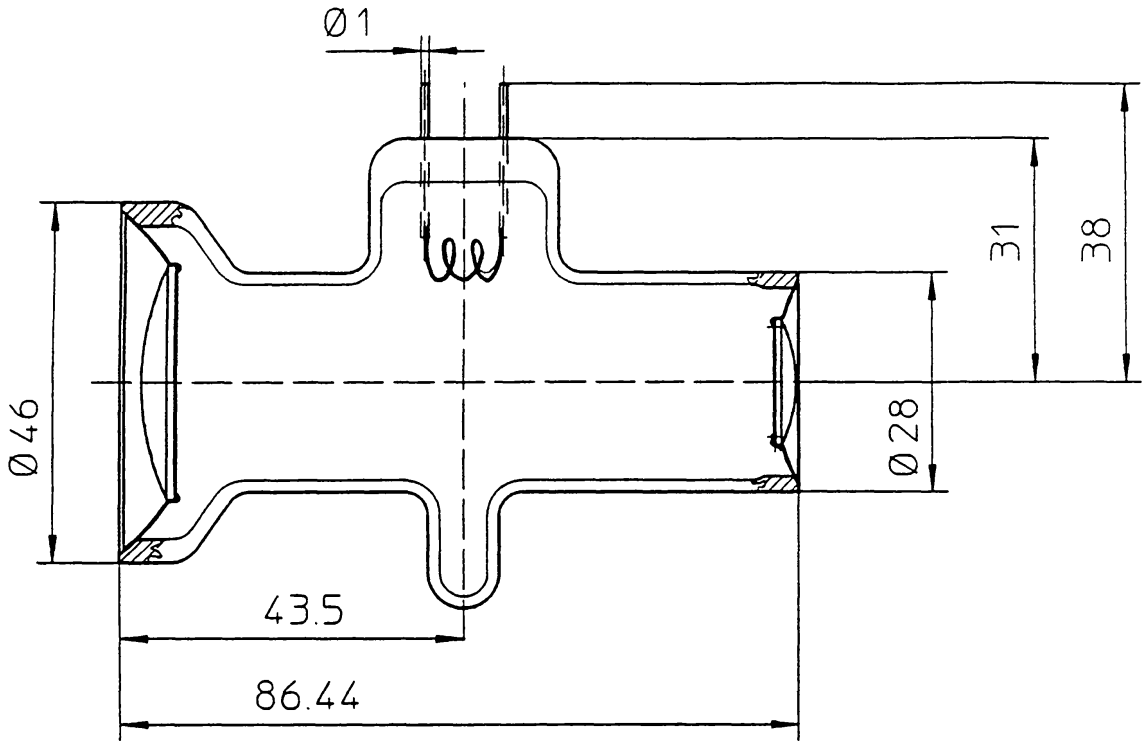

Fig. 14. Schematic of the Hydrogen absorption cell. Sizes are in mm. Only one tungsten filament is represented. Entrance window (left) and exit window are MgF2 lenses, connected to the Pyrex vessel through a silver cup soldered with AgCl.

tion is at the highest point of the emission profile. From the value R_{min} the linewidth, therefore the temperature of the gas could be determined [Bertaux *et al.* , 1977]. When the radial velocity is more than about 30 km/s, absorption is negligible ($R = 1$). With a series of measurements from different directions the Lyman α profile can be retrieved with deconvolution [Quémerais, 1993]. This is the so-called Doppler Angular Spectral Scanning (DASS) method [Bertaux and Lallement, 1984] which allows to retrieve the original line profile from a series of measurements of R on the sky. One has to assume of course that the spectral profile shape is not changing with the direction of sight. It is better verified when a small angle change translates into a large Doppler shift, V_D. Since $V_D = V_r \cos\alpha$, where α is the angle of the direction of sight with V_r, this happens when V_r is large and near $\alpha = 90°$. Each year around the 1st of March, V_r is at its maximum value of 50 km/s.

A modeled reduction factor distribution for a whole sky is represented in figure 17. $R(\theta, \varphi)$ is always inside a sphere of unity and in the simple case of a uniform velocity distribution, has a minimum value along a band perpendicular to the relative velocity vector, the Zero Doppler Shift Circle (ZDSC) [Bertaux and Lallement, 1984].

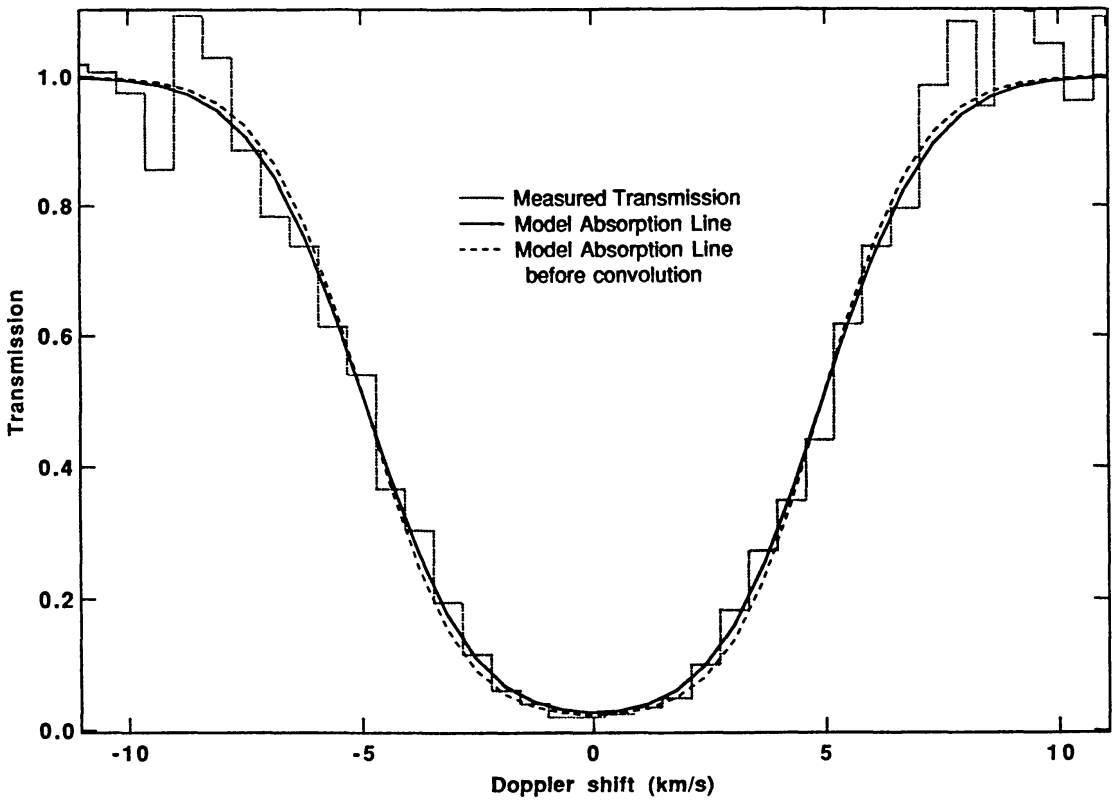

Fig. 15. Measured absorption profile of hydrogen cell SW-11 with a high resolution spectrometer, when operated at a relatively high level of absorption. Dotted sky-line : measurements. Solid line : model fitted to the measurements. Dashed line : same model before convolution by the spectrometer instrumental line profile. The wavelength unit is expressed in km/s, with $\nu = c(\lambda - \lambda_o)/\lambda_o$: 5 km/s = 2×10^{-2} Å = 20 pm ; the equivalent width is 39 mÅ.

From previous measurements with PROGNOZ, we know that the Lyman α linewidth of the interplanetary emission is about 8000 K, and seems to increase for directions of sight larger than 90° from the upwind direction. Radiative transfer inside the interplanetary medium seems to play a role in this increase, but other effects are probably existing.

In principle, H cell measurements are not essential for the primary objective of Solar wind measurements, which may be achieved from a purely photometric mapping. Accordingly, the H cell will not be used permanently. It will be used to consolidate our understanding of the origin of the Lyman α emission by comparing the R pattern with models. In particular, it is possible that the interaction between the solar wind and the interstellar H gas taking place at the heliopause (at 80-100 AU) let an imprint on the velocity distribution of H atoms seen from 1 AU (SOHO), allowing a diagnostic of this interaction (see next section).

In Table 3 are summarized the various regimes of absorption for the SWAN cell numbered SW-12. Each of the two filaments can be activated at a

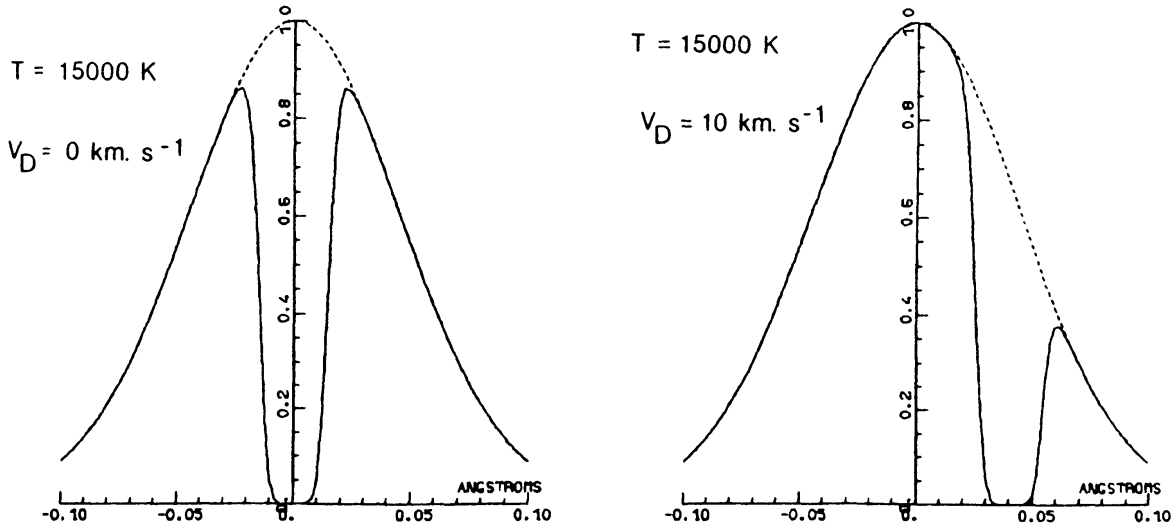

Fig. 16. The effect absorption by a cell with $\tau = 10$ and a cell temperature of 300 K on a gaussian line profile at T = 15000 K is shown for to Doppler shift velocities, $V_D = 0$ and $V_D = 10$ km s−1. The dashed curve is the profile after absorption. The area under the solide line, divided by the total area under the non absorbed line, is the reduction factor R.

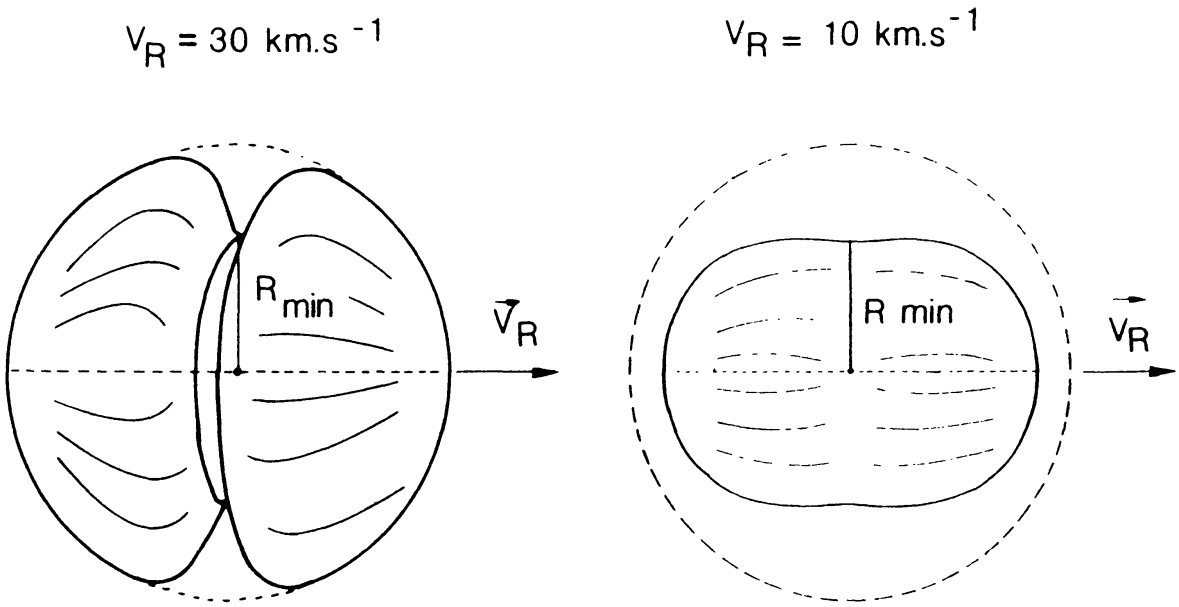

Fig. 17. Predicted pattern of the reduction factor R over the whole celestial sphere, for a gaussian gas, for two values of the relative velocity V_r. For a small value of $V_r = 10$ km/s, there is some absorption every where ($R < 1$). For a larger value of $V_r = 30$ km/s, the absorption is restricted to a band along the Zero Doppler Shift Circle (ZDSC) (after Bertaux and Lallement, 1984).

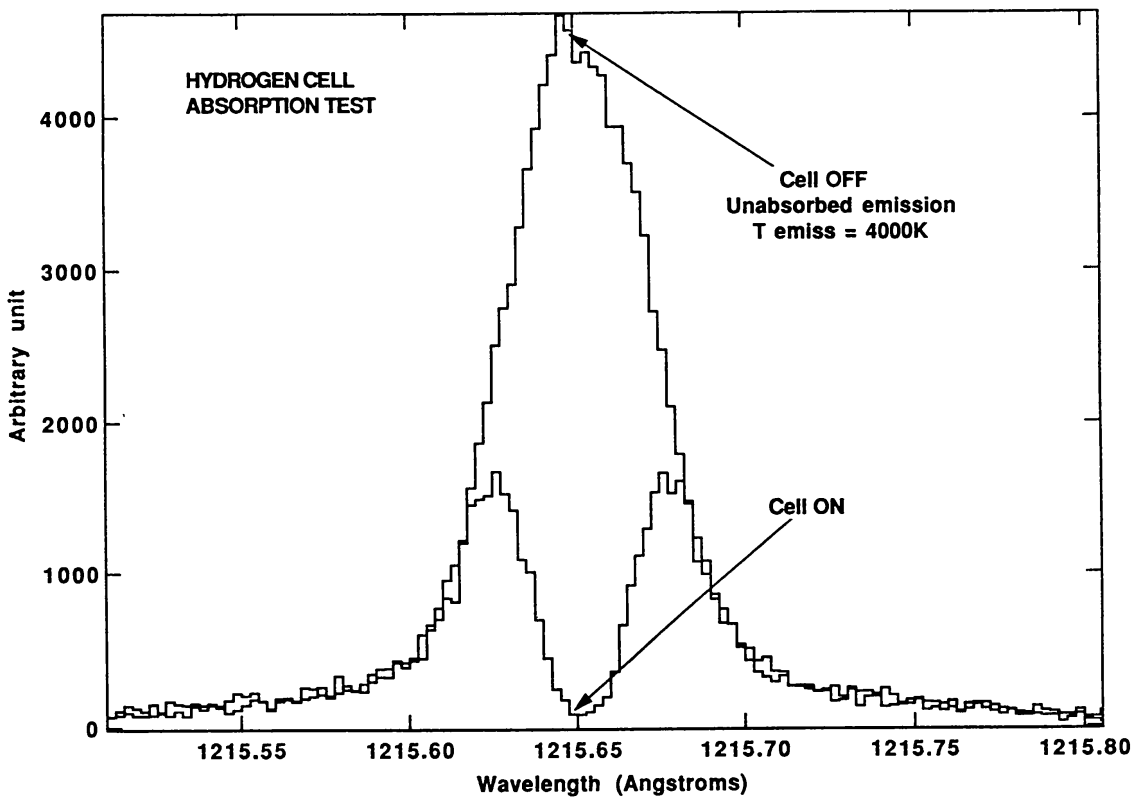

Fig. 18. Two spectra of a hydrogen discharge lamp measured with the 10 meters VUV spectrometer of Observatoire de Meudon, through a SWAN cell # SW-11. OFF : the cell is not operated. ON : the cell is operated at a moderate level. The ratio of the two curves is analyzed on figure 23.

given constant DC regulated voltage. The absorption power is characterized either by the optical thickness at the line center, or by the equivalent width of the absorption profile. This last one was obtained on the ground by using the 10 meter VUV spectrometer of Observatoire de Meudon, and comparing the Lyman α line profile of a discharge lamp, with a resolution of 5×10^{-3} Å seen through an H cell on and off (figure 18).

During the development of SWAN, numerous studies were conducted at Service d'Aéronomie to minimize the aging of the filaments, which lose their Tungsten material when they are switched on. Apparently this is the result of the presence of HCl inside the cell (see above) and cannot be avoided with the present technology of sealing MgF_2 windows with AgCl. Nevertheless, the filaments, which are ribbons of $20 \times 100 \mu$m section, $\approx$ 40 mm long, are thinning relatively slowly, and keep a constant temperature and H production rate while they are aging. The expected lifetime is $\approx$ 2000 hrs of operation, with a 50% on-off duty cycle. Planning of H cell observations should therefore be optimized during the SOHO lifetime. In each cell, one filament will be used preferentially, keeping the second one as a redundant back-up.

TABLE III
TYPICAL H CELL ABSORPTION POWER (SW-12)

Regime	Name	Voltage (volts)	I(mA)	Filament temperature (K)	Equivalent width (mÅ)
Filament 1, Low	F1Low	3.71	420	1282	20
Filament 1, High	F1High	5.71	510	1486	33.8
Filament 2, Low	F2Low	3.46	460	1383	30
Filament 1, High	F2High	4.69	543	1550	38

4.3.6. Photometric Sensitivity and In-Flight Calibration

The number of photons N_p counted in one second for an extended Lyman α source of one Rayleigh in the pixel FOV of 1°, is

$$N_p(1°) = I\ S\ \Omega\ T_c\ T_m^2\ \rho_c\ Q$$
$$1\ \text{Rayleigh} = 10^6/4\pi\ \text{photon cm}^{-2}\ \text{s}^{-1}\ \text{ster}^{-1}$$
$$S = 5.72\ \text{cm}^2\ \text{(entrance pupil)}$$
$$\Omega = (\pi/180)^2 = 3 \times 10^{-4}\ \text{ster (Field of view)}$$
$$S\ \Omega\ (1\ \text{pixel}) = 1.74 \times 10^{-3}\ \text{cm}^2\ \text{ster}$$
$$S\ \Omega\ (25\ \text{pixel}) = 0.043\ \text{cm}^2\ \text{ster}$$
$$T_m^2 = 60\%\ \text{(reflectivity of 2 mirrors at Lyman } \alpha)$$
$$T_c = 20\%\ \text{(transmission of the cell at Lyman } \alpha)$$
$$\rho_c = 0.5,\ Q = 9\%$$
$$N_p(1°, 1\ \text{Rayleigh}) = 0.75\ \text{count/s}$$

With a typical intensity of 500 Rayleigh, the counting rate is 374 for $\rho_c = 50\%$, and with a counting time of 45s, the total number of counts is 17×10^3 yielding a statistical accuracy of 0.8% for one photometric measurement and 1.1% for a reduction factor measurement, which is the desired accuracy.

The number of counts per second for a star depends on the stellar spectrum shape F_λ:

$$N^* = \int_\lambda F_\lambda\ S\ T_\lambda\ Q\ T_m^2\ T_c\ d\lambda \tag{7}$$

where F_λ is in phot.cm^{-2} s^{-1} nm.

Absolute ground calibrations were performed with a synchroton radiation beam (LURE, Orsay) going through a monochromator. The SWAN counting rate was compared with an Aluminum NIST diode, which Q.E. at Lyman α is 1.07% according to the NIST calibration curve.

The sky is full of stars which can serve as a monitoring of the potential sensivity variations of SWAN sensors. Observations of various stars, which short λ cut off varies with the spectral types, will be helpful to see at which wavelength the sensitivity variation occurs. During such an exercise, one will

have to take into account the chromatic aberration, i.e. the image of a star is not a point, but is slightly elongated with a certain wavelength distribution of its light across several pixels of the detector.

5. SWAN Observations Connected with the Heliopause

The heliospause separates the solar wind plasma from the interstellar plasma. There may be also substantial modifications of the neutral hydrogen flow characteristics at the heliospheric interface crossing. The reason for these changes is the coupling with the protons via charge-exchange. Before being deviated and excluded from the heliosphere, the interstellar H^+ are slowed down, heated, and compressed. After charge-exchange with them, the properties of the neutrals are modified towards the properties of the protons. Since the first discussion of this effect [Wallis, 1975], modeling has been carried out in several ways [Baranov and Malama, 1993; Osterbart and Fahr, 1992] and three types of effect are predicted :

(a) the bulk velocity of H neutral is reduced (deceleration effect) at heliopause crossing, whereas neutral He atoms are unaffected.

(b) the H neutral density inside the heliosphere is smaller than outside in the local interstellar medium (filtration effect).

(c) the velocity distribution of H atoms *at infinity* (say, at 40 AU, but well inside the heliopause) is no longer a Maxwellian (perturbation of the velocity distribution). Such a perturbation will persist when H atoms are approaching the sun, and the observed velocity distribution near the sun will be different from what can be expected from a simple "hot" model, with no heliopause effect. Indeed, some H cell Prognoz observations in the downwind hemisphere could not be fitted by any *hot* model [Bertaux *et al.*, 1985].

Several new lines of evidence have emerged, fostering the idea of a relatively nearby heliopause: Gurnett *et al.* [1993]; Cummings, Stone and Webber [1993]; Quémerais *et al.* [1995]. In this case, one expects significant neutral H perturbations [Lallement *et al.*, 1993; Quémerais *et al.*, 1992]. Indeed, there is evidence for a deceleration of H, by comparing its velocity of 20 km s^{-1} inside the solar system measured by Prognoz and more recently Hubble Space Telescope [Lallement *et al.*, 1993], to the helium velocity measured at 26 km s^{-1} by Ulysses [Witte *et al.*, 1993] which coincides exactly with the velocity vector of the Local Interstellar Cloud (LIC), which the Sun is presently traveling through [Lallement and Bertin, 1992; Lallement *et al.*, 1995].

Complete data sets of reduction factor, covering the whole sky at various times of the year (and corresponding Doppler shifts), will be obtained from SWAN, and will be compared with the most realistic H distributions derived from the theory of Baranov and Malama, for which the radiative

transfer equation will also be solved. This will certainly yield an even better understanding on the actual physical conditions near the heliopause, and therefore will also yield its distance from theoretical arguments.

Shall we need to take into account these perturbed velocity/density distribution in the SWAN analysis of solar wind variation with latitude ? The answer is not clear yet. Certainly a first analysis will make use of the classical *hot* model to determine the solar wind distribution, but further work is needed to decide if the heliopause perturbations can be really neglected in the modeling of the solar wind ionization of the interstellar flow of hydrogen.

6. Coronal Observations

According to Withbroe *et al.* [1982], the coronal Lyman α intensity decreases very fast from 7 kR at $4R_S$ down to 1 kR at about 5 R_S. This means that above 5 R_S it becomes comparable and weaker than the interplanetary emission, which is seen through the corona as an additional background, somewhat highly peaked spectrally.

The Sun shade mounted on the spacecraft body will act as an occulting system, allowing SWAN to observe down to about 10 R_S. Since the interplanetary background does not vary significantly over a few degrees, except for a few regions of the sky, SWAN should be able to provide a good correction for the UVCS observations at high altitudes ($R > 5R_S$), where the coronal signal is significantly contaminated. It also should provide an estimate of the coronal Lyman α line-width at these altitudes (in fact, an average over one degree), thanks to the use of the H cell, and this should allow a comparison with the UVCS results and their extrapolation at higher levels.

Another somewhat speculative but interesting possibility for SWAN is to follow in real time the CME's and measure their Lyman α emissivity. The CME's are well known for their Hα emissions, and the processes for these emissions at large distances are not firmly established. Measuring the Lyman α should allow to distinguish between different possible mechanisms. In particular, if recombination is at the origin of a part of the Hα emission, then an equivalent quantity of Lyman α photons should be emitted. These measurements of course would be particularly valuable when correlated with other SOHO observations, i.e. if a CME event is tracked from the solar surface (SUMER) up to a few R_S (UVCS) and above (SWAN).

Finally, it will be extremely interesting to measure the Lyman-α background close to the Sun, because according to calculations by Fahr *et al.* [1981], de-ionization of solar wind on zodiacal dust could produce a detectable additional emission.

7. Observations of Comets

7.1. Monitoring of H/H_2O Gaseous Production

The Lyman α emission is the most intense UV emission in comets: H atoms produced from photodissociation of H_2O, the major volatile component of a cometary nucleus, are directly exposed to the Sun during their expansion into a huge envelope of H: 2×10^7 km for comet Bennett, during the discovery observation of such an envelope [Bertaux and Blamont, 1970 ; Bertaux et al., 1973]. SWAN will be able to monitor the H production of all known comets which become bright enough, and in particular near the sun, when they are generally brightest and cannot be observed either from the ground in the optical domain, or in the UV from IUE or from HST (no observation is possible within $\approx 45°$ from the Sun). A dozen of comets per year is a typical number that SWAN could follow. In some cases, a continuous Lyman α monitoring may reveal the period of rotation, as in the case of Halley's comet when its Lyman α emission was observed with Pioneer Venus UV spectrometer [Stewart, 1987]. Of particular interest will be the periodic comets which are candidates for a rendez-vous exploration by ESA Rosetta mission, namely Wirtannen comet.

The use of the absorption H cell allows to study with great refinement the velocity of cometary H atoms, when Doppler effect conditions are adequate (when distance Earth Comet goes through an extremum). In order to deduce the production rate of H, $Q(H)$, from an intensity measurement of Lyman α it is necessary to know the expansion velocity v of the atoms. $N(p)$, the column density at distance p, is equal to $Q/(4vp)$ and is proportional to the Lyman α emission rate (at least in the optically thin regime).

Up to now, the velocity has not been measured directly, and it is assumed that it results from the residual energy left to H after photodissociation of H_2O and OH, with an estimate of about 20 and 8 km s^{-1}. Of course a safer estimate of the production rate would be achieved by measuring directly v, which could also perhaps discriminate several populations of H atoms of different origin (i.e., organic material within the dust grainsi [Kissel *et al.*, 1986]).

Because SWAN can observe relatively faint comets, and near the sun when they cannot be oserved from the ground, SWAN could detect some new comets before they are discovered from ground based observations. A simulation was conducted [Berthé, 1995] for all the new comets which were discovered during the year 1992. A crude estimate for their Lyman α emission rate was derived from an empirical relationship between the visual magnitude m'_v of the comet and its production rate $Q(H)$ [Roettger *et al.* , 1990]. Then the average Lyman α brightness in the 1° FOV of a SWAN pixel was estimated for all the new comets of 1992 as a function of time taking m'_v from IAU circulars. If SWAN had been in flight during the year 1992, the 10

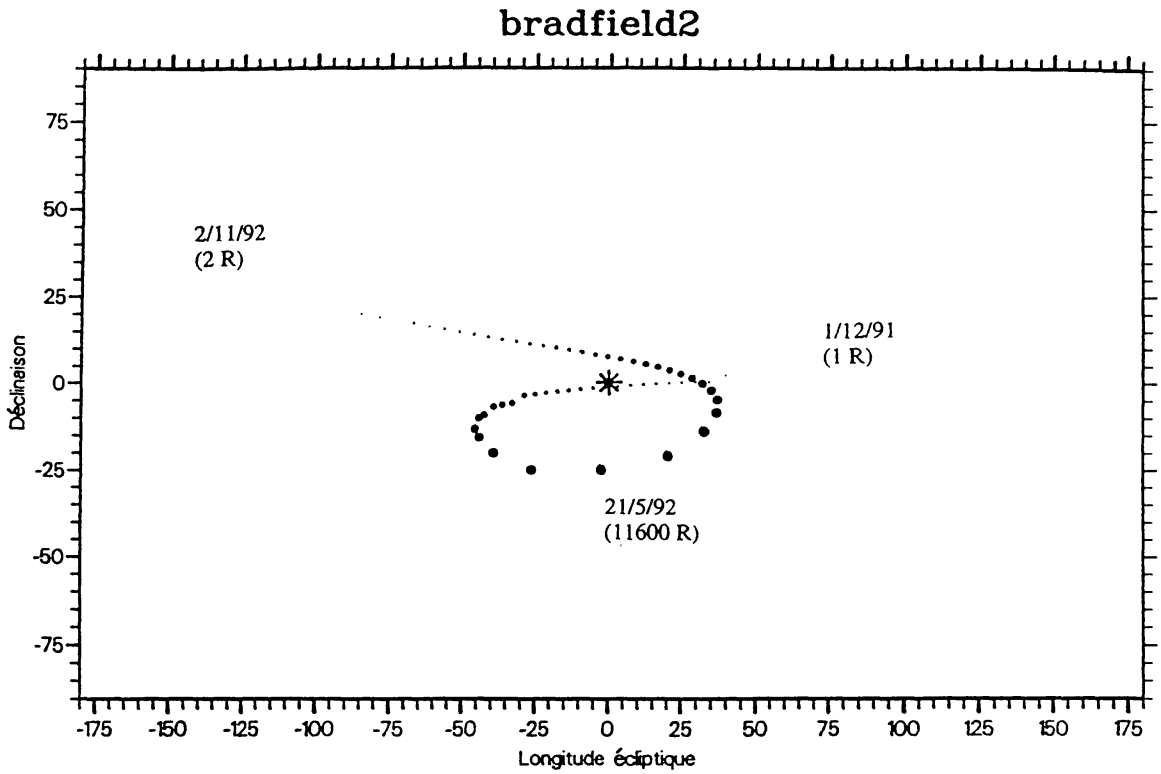

Fig. 19. Apparent trajectory of comet Bradfield 2, as seen from L1 point in an ecliptic system centered on the Sun (represented by a star). The size of the dot grows as the algorithm of the predicted Lyman α intensity, which is indicated for several dates. Because of its proximity to the Sun, it could have been observed by SWAN before being seen from Earth.

Rayleigh intensity detection limit in 45 s, would have been reached before the first ground based observation date for nine comets out of 20 comets (new or periodic) in 1992. The most spectacular example is displayed on figure 19, for the simulation of comet Bradfield 2. A signal of 100 R would have been reached on March 30, 1992, whereas the comet was first observed from ground two months later, on May 31, 1992. At this time the Lyman α intensity was more than 11 kR. Therefore, systematic SWAN observations of a region near the Sun (say, at $\approx 25°$) might reveal the presence of a comet before it would be discovered from the ground.

8. Observations of the Geocorona

Produced by photodissociation of H_2O in the upper atmosphere of the Earth, geocoronal H extends into the exosphere to more than 10^5 km of distance. The geocoronal intensity varies from 25 kiloRayleigh on the sunlit Earth disc, down to 100 Rayleigh at 10^5 km. As seen from SOHO halo orbit at 1.5×10^6 km, this Lyman α spot extends over 15° of diameter, usually at $\approx$ 24° from the anti-solar direction. The Earth covers less than 1 pixel. Every

other day, we will make a cartography of the geocorona with a resolution of 1° allowing to monitor the global features of the geocorona. The average exospheric temperature and density distribution will be monitored as a function of solar activity, at a time of moderate solar activity. Such a study could be compared to a similar one already done at a time of high solar activity with OGO-5 in 1968-69, in which it was found that, in addition to the normal Jeans's thermal escape, there was a non-thermal escape of H varying also with solar activity [Bertaux, 1975]. This clearly addresses to the Solar Terrestrial relationship whitin the frame of the ISTP programme, to which the SOHO-Cluster ESA cornerstone is dedicated. H cell absorption measurements will allow a direct determination of the temperature in the exosphere. The solar Lyman α radiation pressure acts on exospheric H atoms, and in average push them in the anti-solar direction, which creates an extension of the geocorona already observed and called *geotail* by Thomas and Bohlin [1972]. Because of Earth's orbital motion, this geotail is likely *trailing*, in such a way that as seen from SOHO it will be more extended in the direction ooposite to the Earth's orbital motion.

9. Observations of the Solar Lyman α Profile Variations

By averaging solar Lyman α spectral profiles taken over many points of the solar disk, SUMER will be able to provide high resolution profiles of the solar Lyman α line as observed with OSO-8 [Artzner, 1982]. Such global average profiles could serve the interpretation of SWAN Lyman α maps, since in the modeling of backscattered interplanetary Lyman α , the exact solar line profile can be introduced. Because of the 20 km s^{-1} velocity of the interstellar wind, each atom according to its position in the interplanetary medium is excited by a slightly different part of the solar line spectrum, over the range of $\pm$ 20 km/s or $\pm$ 0.08 Å.

On the other hand, the interplanetary hydrogen acts like a high resolution spectrometer for the study of the integrated disc solar time profile and we have all the ingredients to detect solar oscillations around H Ly-α line center. Here, the interplanetary hydrogen acts as a gigantic resonance cell, like in the classical experiment of Grec *et al.* [1980] on the sodium D line, in which they discovered many modes of the 5 min. global oscillations with the use of a sodium resonance cell.

Since there are two sensor units, they can be maintained in two different sky directions, which would respond to two different *sides* of the sun. In particular, looking at the ecliptic poles would provide a response to one global single hemisphere, North or South, or both simultaneously.

Acknowledgements

The construction of the SWAN space instrument required the help of many people at various stages. We wish to thank particularly Peter Jenssen, Claude Berner and Ron Thomas at ESA, Jean-Pierre d'Allest, who as Directeur General made possible the participation of CNES to SWAN, once the instrument was selected by ESA; Dr. Okano from Tohoku University (Japan) who made some early measurements of H cell absorption profile with synchrotron radiation, MM. Michaud, Salvetat and Delaboudinière at IAS, for providing the vacuum facilities for testing SWAN with Synchrotron radiation, Mrs Bernard, G. Chrétiennot and M. Leclère at Service d'Aéronomie for their participation to H cell fabrication and testing, G. Souchon for photomultiplier evaluation, Ms. Leveau at Service d'Aéronomie for typing many SWAN documents, including this paper, and C. Cardon for bibliography, Franoise Genova at CNES for her support and Mrs. Launay at Observatoire de Meudon for providing the 10 m VUV spectrometer facility. SWAN was financed in France by CNES with support from CNRS and in Finland by TEKES and the Finnish Meteorological Institute.

References

Ajello J.M., Pryor W.R., Barth C.A., Hord C.W., Stewart A.I.F., Simmons K.E., Hall D.T.: 1994, *Astron. Astrophys.*, **289**, 283-303
Ajello J.M., Stewart A.I., Thomas G.E., Graps A.: 1987, *Astrophys. J.*, **317**, 964-986
Artzner, G: 1982, Thèse de doctorat d'Etat, Université de Paris 7
Baranov V.B., Malama Yu. G.: 1993, *J. Geophys. Res.*, **98, A9**, 15,157-15,163
Bertaux J.L.: 1975, *J. Geophys. Res.*, **80**, 639-642
Bertaux J.L., Blamont J.E.: 1970, *C.R. A.S.*, **270**, 1581-1584
Bertaux J.L., Blamont J.E., Mironova E.N., Kurt V.G., Bourgin M.C.: 1977, *Nature*, **270**, 156-158
Bertaux J.L., Blamont J.E., Festou M.: 1973, *Astron. Astrophys.*, **25**, 415-430
Bertaux J.L., Blamont J.E.: 1971, *Astron. Astrophys.*, **11**, 200-217
Bertaux J.L., Lallement R.: 1984, *Astron. Astrophys.*, **140**, 230-242
Bertaux J.L., Lallement R., Kurt V.G., and Mironova E.N.: 1985, **Astron. Astrophys.**, **150**, 1-20
Berthé M., Ph.D. Thesis, Université de Paris 6, January 1995
Blum P.W. and Fahr H.J.: 1970, *Astron. Astrophys.*, **4**, 280
Blum P., Gangopadhyay P., Ogawa H.S., and Judge D.L.: 1993, *Astron. Astrophys.*, **272**, 554
Bzowski M. and Rucinski D.: 1995, *Space Science Rev.*, **72**, 467-470
Cook J.W., Meier R.R., Bruekner G.D., Van Hoosier M.E.: 1981, *Astron. Astrophys.*, **97**, 394
Cummings A.C., Stone E.C., Webber W.R.: 1993, *J. Geophys. Res.*, **98, A9**, 15165-15168
Fahr H.J., Ripken H.W. and Lay G.: 1981, *Astron. Astrophys.*, **102**, 359
Fite W.L., Smith A.C.H. and Stebbings R.F.: 1962, *Proc. Roy. Soc. A.*, **268**, 527
Grec G., Fossat E., Pomerantz M.: 1980, *Nature*, **288**, 541
Gurnett D.A., Kurth W.S., Allendorf S.C., Poynter R.L.: 1993, *Science*, **262**, 199
Holzer T.E., Lallement R., Munro R.H.: 1986, *J. Geophys. Res.*, **91**, 6751-6759
Holzer T.E., Leer E.: 1980, *J. Geophys. Res.*, **85**, 4665

Huomo H., Hannula H., Viherkanto K.: 1992, *Proc. Fifth European Space Mechanism and Tribology Symposium*, ESA SP-334
Joselyn J.A. and Holzer T.E.: 1975, *J. Geophys. Res.*, **80**, 903
Kissel J., Sagdeev R.Z., Bertaux J.L. *et al.*: 1986, *Nature*, **321**, 280
Kojima M., Kakinuma T.: 1987, *J. Geophys. Res.*, **92, A7**, 7269-7279
Kumar S., Broadfoot A.L.: 1979, *Astrophys. J.*, **228**, 302-311
Kyrölä E., Summanen T. and Raback P.: 1994, *Astron. Astrophys.*, **288**, 299-314
Lallement R., Bertaux J.L., Kurt V.G., Mironova E.N.: 1984, *Astron. Astrophys.*, **140**, 243
Lallement R., Bertin P.: 1993, *Astron. Astrophys.*, **266**, 479-485
Lallement R., Bertaux J.L., Dalaudier F.: 1985, *Astron. Astrophys.*, **150**, 21
Lallement R., Holzer T.E., Munro R.H.: 1986, *J. Geophys. Res.*, **91**, 6751
Lallement R., Bertaux J.L.: 1990, *Astron. Astrophys.*, **231**, L3
Lallement R., Bertaux J.L., Clarke J.T.: 1993, *Science*, **260**, 1095
Lallement R., Bertaux, J.L., Kurt V.G.: 1985, *J. Geophys. Res.*, **90**, 1413
Lallement R., Kyrölä E. and Summanen T., *Space Science Rev.*, **72**, 455
Lallement R., Malama Yu. G., Quémerais E., Bertaux J.L., Zaitsev, N.A.: 1992, *Astrophys. J.*, **396**, 696
Lallement R., Stewart I.A.: 1990, *Astron. Astrophys.*, **227**, 608
Lallement R.: 1987, *Solar Wind 6*, NCAR/TN-306, 651
Leer E., Holzer T.E., Fla T.: 1982, *Space Sci. Rev.*, **33**, 161-200
Munro R.H., Jackson B.V.: 1977, *Astrophys. J.*, **213**, 874
Osterbart R., Fahr H.J.: 1992, *Astron. Astrophys.*, **264**, 260
Pryor W.R., Ajello J.M., Barth C.A., *et al.* : 1992, *Astrophys. J.*, **394**, 363-377
Quémerais E. and Bertaux J.L.: 1993, *Astron. Astrophys.*, **277**, 283
Quémerais E., Lallement R., Bertaux, J.L.: 1993, *J. of Geophys. Res.*, **98, A9**, 15199-15210
Quémerais E.: 1993, Ph.D. Thesis, Université Paris VI
Quémerais E., Lallement R. and Bertaux J.L.: 1992, *Astron. Astrophys.*, **265**, 806-816
Quémerais E., Sandel B.R., Lallement R. and Bertaux J.L.: 1995, *Astron. Astrophys.*, **299**, 249
Richardson J.D., Paularena K.I., Belcher J.W. and Lazarus A.J.: 1994, *Geophys. Res. Lett.*, **21**, 14, 1559
Roettger E.E., Feldman P.D., A'Hearn M.F. and Festou M.C.: 1990, *Icarus*, **86**, 100
Stewart A.I.F.: 1987, *Astron. Astrophys.*, **187**, 369-374
Summanen T., Lallement R., Bertaux J.L. and Kyrölä E.: 1993, *J. Geophys. Res.*, **98, A8**, 13215-13224
Thomas G.E. and Krassa R.F.: 1971, *Astron. Astrophys.*, **11**, 218
Thomas G.E. and Bohlin R.: 1972, *J. Geophys. Res.*, **77**, 16, 2752-61
Wallis M.K.: 1975, *Nature*, **254**, 202
Withbroe G.L., Kohl J.L., Weiser H., Munro R.H.: 1982, *Space Science Reviews*, **33**, 17
Witte M., Rosenbauer H., Banaszkiewicz M., Fahr H.J.: 1993, *Adv. Space Res.*, **13**, 6, 121